

ESTIMATION OF THE SOURCE MECHANISMS OF
MICROSEISMIC EVENTS FROM A BARNETT SHALE
PLAY

A Thesis Presented to the Faculty of the
Department of Earth and Atmospheric Sciences
University of Houston

In Partial Fulfillment
of the Requirements for the Degree
Master of Science

By
Emmanuel Olisejindu Osakwe
May 2013

ESTIMATION OF THE SOURCE MECHANISMS OF
MICROSEISMIC EVENTS FROM A BARNETT SHALE
PLAY

Emmanuel Olisejindu Osakwe

APPROVED:

Dr. Evgeni Chesnokov, Chairman

Dr. John Castagna

Dr. Donald Kouri

Dr. Dan Wells, Dean

College of Natural Sciences and Mathematics

ACKNOWLEDGEMENTS

I would like to express my heartfelt appreciation to Dr. Evgeni Chesnokov whose tutelage and fatherly advice was instrumental to the completion of this project. I would also like to thank Dr. Donald Kouri for the instructions he gave during our weekly seminar, and for his suggestions. I would not forget to mention Zhao Li for helping me with the writing of the codes for the synthetic Green's function in isotropic medium. Thanks to Dr. Maria Krasnova for supplying me with the software for analyzing seismograms. I am also grateful to members of my thesis group whose weekly talks, and constructive input at the seminar provided some helpful leads in arriving at some of my results. I wish you all the best in your future endeavors.

ESTIMATION OF THE SOURCE MECHANISMS OF
MICROSEISMIC EVENTS FROM A BARNETT SHALE
PLAY

An Abstract of a Thesis

Presented to

the Faculty of the Department of Earth and Atmospheric Sciences

University of Houston

In Partial Fulfillment

of the Requirements for the Degree

Master of Science

By

Emmanuel Olisejindu Osakwe

May 2013

Abstract

The waveforms generated during hydraulic fracturing in unconventional oil and gas reservoirs contain information about the nature of the failures that gave rise to the observed wave fields. Inverting for the moment tensor has become an important way of gaining understanding of the fracturing process. Microseismic events recorded off of a Barnett shale play were first subjected to power spectra density analysis in order to determine the frequency content of the events. The analysis revealed that the peak energy of the first arrivals was in range 100 – 800 Hz, and no signal of significant energy was found beyond 900 Hz. The inversion for the moment tensor of about 100 of these events, which were of good enough quality, was then carried out. The moment tensor revealed that the source mechanisms of most of the events were predominantly shear failures, with a few of the events being of non-shear-type failure like compensated linear vector dipoles (CLVD). The condition number of the sensitivity matrix used for the inversion was somewhat high, even for a constrained inversion. The fact that the data were recorded from an array of geophones in a single borehole might be the reason for the unstable inversion, since data recorded from a single borehole cannot resolve all the six independent elements of the moment tensor.

Table of Contents

Abstract.....	v
Table of Contents.....	vi
List of Figures.....	viii
Chapter One.....	1
1.1 INTRODUCTION.....	1
1.2 FOCAL MECHANISM.....	2
1.3 FOCAL MECHANISM DETERMINATION.....	5
Chapter Two.....	8
2.1 INTRODUCTION.....	8
2.2 THE SEISMIC MOMENT TENSOR.....	8
2.3 METHODS OF SEISMIC MOMENT TENSOR INVERSION.....	9
2.4 WHAT DETERMINES THE STABILITY OF THE INVERSION?... 10	
2.5 GRAPHICAL REPRESENTATION OF SOURCE MECHANISMS.. 13	
2.5.1 BEACH BALL DIAGRAMS.....	13
2.5.2 SOURCE TYPE PLOTS.....	15
Chapter Three.....	17
3.1 INTRODUCTION.....	17
3.2 ANALYSIS OF THE DATA.....	20
3.3 POWER SPECTRAL DENSITY ANALYSIS.....	21
3.4 THE ELASTODYNAMIC GREEN’S FUNCTION.....	29
3.4.1 THE EQUATION OF MOTION.....	29
3.5 FOCAL MECHANISM DETERMINATION OF THE EVENTS.....	33
3.5.1 ISOTROPIC CASE.....	33
3.5.2 VERTICAL TRANSVERSE ISOTROPIC (VTI) CASE.....	35

Chapter Four.....	39
4.1 INTRODUCTION.....	39
4.2 ANALYSIS OF RESULTS.....	41
Chapter Five.....	44
5.1 INTRODUCTION.....	44
5.2 CHALLENGES.....	44
5.3 RECOMMENDATIONS.....	46
References.....	47

List of Figures

Figure 2.1: Condition number as a function of solid angle.....	12
Figure 2.2: An equal area stereonet.....	14
Figure 2.3: Beach balls and their associated moment tensors.....	15
Figure 2.4: A source type plot.....	16
Figure 3.1: A schematic of the acquisition geometry of the microseismic events.....	17
Figure 3.2: A cross section of the medium that was hydraulically fractured, and from which microseismic events were recorded.....	18
Figure 3.3a: Waveform of event X.....	19
Figure 3.3b: Waveform of event A.....	20
Figure 3.4a: Periodogram of event X for frequencies 0 – 1,000 Hz.....	22
Figure 3.4b: Periodogram of event X for frequencies 1,000 – 2,000 Hz.....	23
Figure 3.5a: Periodogram of event A for frequencies 0 – 1,000 Hz.....	24
Figure 3.5b: Periodogram of event X for frequencies 1,000 – 2,000 Hz.....	24
Figure 3.6a: Periodogram of first quarter time recording of event A.....	25
Figure 3.6b: Periodogram of second and third quarter time recording of event A.....	26
Figure 3.7a: Periodogram of first quarter time recording of event X.....	26
Figure 3.7b: Periodogram of second and third quarter time recording of event X.....	27
Figure 3.8a: Comparison of event 047 before and after filtering (Vertical component).....	28

Figure 3.8b: Comparison of event 047 before and after filtering (Horizontal component)	28
Figure 3.9: Velocity model for the isotropic case	34
Figure 3.10: Velocity model for the VTI case	37
Figure 4.1: Waveform of event B	40
Figure 4.2a: Periodogram of event B for frequencies 0 – 800 Hz	40
Figure 4.2b: Periodogram of event B for frequencies 900 – 2,000 Hz	41
Figure 5.1: Typical nature of most of the data	45

Chapter One

1.1 INTRODUCTION

Earlier discoveries of oil and gas resources were predominantly on porous and permeable sedimentary (sandstones and carbonates) rocks. It was not uncommon to find reservoirs with porosity as high as 30% or more, and permeability was in the millidarcy regime. However, most modern day reservoirs, especially in the United States, are to be found mostly in shale formations. They are often tight formations, with permeability in the microdarcy, and sometimes in the nanodarcy scale. As a result, a common practice in most modern day oil and gas reservoirs is hydraulic fracturing. Hydraulic fracturing is the propagation of fractures in a rock layer caused by the presence of a pressurized fluid (often times, water). Induced hydraulic fracturing or hydro-fracking, commonly known as fracking, is a technique used to release petroleum, natural gas (including shale gas, tight gas, and coal seam gas), or other substances for extraction. (Charlez, 1997) The intent of this process is to enhance subsurface fracture systems so as to allow oil and gas to move more freely from rock pores to production wells, which bring the oil and gas to the surface. Because of growing concerns amongst people over the environmental hazards that hydraulic fracturing might pose, various methods have been put in place to monitor the pressure and growth rate of the resulting fractures. One of the methods used is microseismic monitoring. The injection of high pressure fluids into the ground generates seismic waves; hence, technically speaking, hydraulic fracturing causes earthquakes. However, the moment magnitude M_w of the resultant earthquake, which is a measure of the strength of an earthquake, is often too small to be

detected at the surface (M_w values are typically less than zero for micro-earthquakes [Šíleny *et al.*, 2009]); hence they are referred to as micro-earthquakes.

The aim of this study is to determine the focal mechanism of a set of induced micro-earthquakes recorded off of a Barnett shale play. In doing this, we are able to deduce the kind of failures at the source rocks that gave rise to the observed wave fields. This, in turn, provides us with information on how the fractures are propagating in the rock formation, the state of the in situ stress, which in turn can serve as a guide on how to maximize reservoir permeability for enhanced production. (Baig and Urbancic, 2010; Šíleny *et al.*, 2009)

1.2 FOCAL MECHANISM

Microseismic monitoring has become a very useful tool in the oil and gas industry for mapping of the propagation of fractures caused by hydraulic fracturing. The concept of focal mechanism, a well established concept in global seismology, is the theoretical framework by which effective microseismic monitoring is carried out (Sipkin, 1994). The focal mechanism of an earthquake is a geometrical or mathematical description of the type of deformation at the source region that gave rise to an observed seismic wave. It also describes the orientation of the fault plane and the slip vector, from which we can deduce the nature of the failure that generated the observed seismic wave. The focal mechanism solution can be represented graphically as a beach-ball diagram, which is a lower hemisphere stereographic projection. Beach-ball diagrams

have been used to derive the event location of microseismic events from hydraulic fracturing (Baig and Urbancic, 2010).

In any wave propagation phenomenon, when the distance of observation and the wavelength of the wave are much greater than the dimension of the source region, the wave source can be approximated as a point source. This also applies to seismic wave sources in which case the source region would be the fault planes or the rock bodies where the seismic waves originate from. The seismic moment tensor can be used to describe sources of this nature (Herrmann, 1975). The rock bodies at the source, having been under stress, undergo failure as a way of stress relief which is released in form of seismic waves.

The displacement at the far field due to a point source can be estimated using the expression (Aki and Richards, 2002)

$$U_n(\mathbf{x}, t) = M_{ij}(t) * \frac{\partial}{\partial \xi_j} G_{ni}(\mathbf{x}, t; \boldsymbol{\xi}, 0) \dots (1.1)$$

where \mathbf{x} is the position of the recording station, $\boldsymbol{\xi}$ is the location of the source. $M_{ij}(t)$ are the components of the time dependent moment tensor of the seismic source, and G_{ni} is the elastodynamic Green's function that contains information about the wave propagation between \mathbf{x} and $\boldsymbol{\xi}$. The subscript n is related to the component of the ground motion at the receiver position. The symbol $*$ denotes temporal convolution.

For a moment tensor with components that have the same time dependence, the time dependent moment tensor can be written in terms of a source time function and a time independent moment tensor (Madariaga, 2007). Hence, we can rewrite (1.1)

$$U_n(\mathbf{x}, t) = M_{ij} \left[s(t) * \frac{\partial}{\partial \xi_j} G_{ni}(x, t; \xi, 0) \right] \dots (1.2)$$

where M_{ij} are the components of the time independent moment tensor and $s(t)$ is the source time function (Rodriguez *et al.*, 2011). We can further write this as

$$U_n(\mathbf{x}, t) = M_{ij} G_{ni,j}(x, t; \xi, 0) \dots (1.3)$$

In matrix form, this becomes

$$\mathbf{u} = \mathbf{G}\mathbf{m} \dots (1.4)$$

where \mathbf{m} is a matrix whose elements are the six independent elements of the time independent moment tensor, and \mathbf{G} is the Green's tensor matrix. By building a library of Green's function from a reliable velocity model of the region of study, we can invert for the complete moment tensor components. (Li *et al.*, 2011; Li *et al.*, 2009) We shall discuss more about the Green's function later on.

We obtain the moment tensor, \mathbf{m} , which is a description of the source mechanism by carrying out the following operation:

$$\mathbf{m} = \mathbf{G}^+ \mathbf{u} \dots (1.5)$$

where

$$\mathbf{G}^+ = (\mathbf{G}^T \mathbf{G})^{-1} \mathbf{G}^T \dots (1.6)$$

is known as the generalized inverse of \mathbf{G} . The generalized inverse, also known as pseudo-inverse, is used because the rectangular nature of \mathbf{G} makes it non-invertible. Assuming the matrix \mathbf{G} is “well-behaved” and properly conditioned, we can obtain the six independent element of the moment tensor from which we can deduce the source mechanism.

1.3 FOCAL MECHANISM DETERMINATION

The process of source mechanism estimation for microseismic events can be broken down into three steps (Chapman and Leaney, 2012), i) determination of the moment tensor of the source, ii) subsequent decomposition of the moment into parameters with physical meaning, and iii) display of these parameter.

(I) The above inversion (equation 1.5) yields a moment tensor of the form:

$$\mathbf{M} = M_o \begin{bmatrix} m_{11} & m_{12} & m_{13} \\ m_{12} & m_{22} & m_{23} \\ m_{13} & m_{23} & m_{33} \end{bmatrix}$$

From the moment tensor, it can be deduced if the source mechanism is purely isotropic or purely deviatoric or a combination of both. If we obtain a moment tensor whose elements are such that the diagonal elements m_{11} , m_{22} , m_{33} are equal and non-zero, then we have a purely isotropic source which represents either an explosion [for $\text{trace}(\mathbf{M}) > 0$] or an implosion [for $\text{trace}(\mathbf{M}) < 0$]. Such a purely isotropic source is

usually as a result of human activity such as mining or nuclear explosion. Hence, moment tensor inversion can be a useful tool for monitoring nuclear activity. (Stein and Wysession, 2003) In reality, though most seismic sources with moment tensors whose trace is non-vanishing do not have equal eigenvalues. A moment tensor with non-vanishing trace and with three unequal eigenvalues is composed of a number of source mechanisms.

(II) The process of decomposition of the seismic moment tensor to obtain the various mechanisms starts with the diagonalization of the moment tensor matrix. When this is done, the moment tensor has its eigenvalues as the only non-zero entries at its leading diagonal; all other entries are zero. Then, we split the moment tensor into an isotropic (first term on the RHS) and deviatoric (second term) component (Jost and Herrmann, 1989)

$$\mathbf{m} = \frac{1}{3} \begin{bmatrix} tr(\mathbf{M}) & 0 & 0 \\ 0 & tr(\mathbf{M}) & 0 \\ 0 & 0 & tr(\mathbf{M}) \end{bmatrix} + \begin{bmatrix} m_1^* & 0 & 0 \\ 0 & m_2^* & 0 \\ 0 & 0 & m_3^* \end{bmatrix}$$

$$= \frac{1}{3} \begin{bmatrix} tr(\mathbf{M}) & 0 & 0 \\ 0 & tr(\mathbf{M}) & 0 \\ 0 & 0 & tr(\mathbf{M}) \end{bmatrix} + \sum_{i=1}^N \bar{m}_i \dots (1.7)$$

where

$$m_i^* = m_i - \frac{m_1 + m_2 + m_3}{3} = m_i - \frac{1}{3} tr(\mathbf{M}) \dots (1.8)$$

The deviatoric part can be decomposed further, but the decomposition scheme from this point is somewhat subjective.

(III) The mechanisms that can be extracted from the deviatoric moment tensor are the double couple (DC) and the compensated linear vector dipole (CLVD) components. A common property of these mechanisms, i.e. DC's and CLVD's, is that their moment tensor has zero trace. This implies that, unlike the isotropic part, the DC and CLVD are not accompanied by volume change.

As discussed earlier, the source mechanisms of a microseismic event can be obtained from inverting for, and subsequent decomposition of, the moment tensor. It is also possible to determine the ratio DC to CLVD contained in the deviatoric moment tensor using the parameter ε which is defined as

$$\varepsilon = \left| \frac{m_{min}^*}{m_{max}^*} \right| \dots (1.9)$$

where m_{min}^* and m_{max}^* are values of the minimum and maximum eigenvalues, respectively, of the deviatoric moment tensor. (Jost and Herrmann, 1989) From this, we can deduce that, for $\varepsilon = 0$, we have a pure double couple, and for $\varepsilon = 0.5$, we have a pure CLVD.

Chapter Two

2.1 INTRODUCTION

An area of intense research interest in seismology is in finding an accurate description of the physics of seismic sources. At first, earthquakes were thought of as simple explosions, then as single force couples, then later as double couples.

(Madariaga, 2007) A common approach is to model seismic sources as equivalent body forces, which are defined as forces “producing displacements at the earth’s surface that are identical to those from the actual forces of the physical process at the source”. (Jost and Herrmann, 1989) A mathematical description of equivalent body forces is the seismic moment tensor.

2.2 THE SEISMIC MOMENT TENSOR

The seismic moment tensor provides a succinct way of representing various seismic sources rather than assuming that sources are due to slip on a fault. It also has the added advantage of affording a means of estimating source mechanism from seismogram inversion. (Stein and Wysession, 2003) Since the work of Gilbert (1970) moment tensor has been used for representing, to a first order approximation, equivalent body forces of general seismic point sources. This representation has made it possible to invert the waveform of an earthquake to obtain its source mechanism. The seismic moment tensor is a second-rank tensor which can model forces representing a sudden

shear dislocation on a fault plane (double couple source), and volumetric explosion or implosion. (Jost and Herrmann, 1989)

2.3 METHODS OF SEISMIC MOMENT TENSOR INVERSION

A number of authors have proposed a wide variety of methods for estimating source mechanism via moment tensor inversion. Wéber (2009) proposed a method of retrieving the time invariant moment tensor and source time function from the time dependent moment tensor estimated from linear inversion of three component waveform. Though the method is non-linear, when applied to synthetic data, it gave good results for both simple and complicated sources.

Gharti *et al.* (2011) employed time reversal imaging techniques for the processing and analysis of microseismic data. A synthetic test of the method showed that it could be used to simultaneously estimate source location and seismic moment tensor. Though the computational demand of this technique is somewhat high, this is offset by its compliancy to parallel processing. An inversion scheme wherein microseismic data recorded by a network of three component geophones is assumed to be representative of the sum of compressive and shear wave arrivals. (Leaney, 2008) Through a process known as least-squares time reversal, the modifications to the source time function due to propagation from source to receiver, are mathematically reversed by least squares inversion.

Li *et al.* (2009) developed a high frequency, full-waveform matching method, and used it in the study of the focal mechanism of micro-earthquakes induced in an oil

field. The method is especially robust for use on surface and borehole microseismic data obtained from a sparse network of receivers, even when a few of the first *P*-wave arrival polarities are not identifiable because of noise contamination, or when only the vertical components are usable.

2.4 WHAT DETERMINES THE STABILITY OF THE INVERSION

At this juncture, we might ask: “How well the moment tensor obtained from inversion does represents the source mechanism that gave rise to an observed wave field. Is it a true representation of the actual failure mode at the source?” A major factor in answering that question, as demonstrated both theoretically and experimentally, is how widespread the receivers are stationed with respect to the source location. Multiple down-hole monitoring arrays in favorable configurations have been shown to reveal details of the source mechanisms such as the style of deformation and fracture orientation. (Baig *et al.*, 2011; Nolen-Hoeksema and Ruff, 1999) A synthetic study done on the geometrical conditions necessary for obtaining a sound moment tensor solutions for microseismic events shows that, a receiver array geometry that subtends a non-zero solid angle, when viewed from the source, would produce the most reliable moment tensor solutions. (Eaton, 2009) In other words, an array of receivers in a single monitoring borehole cannot sufficiently resolve all the six independent elements of the moment tensor, as has been shown in synthetic and experimental studies. (Vavryčuk, 2007; Nolen-Hoeksema and Ruff, 2001, Nolen-Hoeksema and Ruff, 1999) At best, only five of the six independent elements can be retrieved from such an array, and this

requires the use three component sensors that can record amplitudes of both P- and S-waves. (Vavryčuk, 2007, Nolen-Hoeksema and Ruff, 2001; Eaton, 2009)

Another factor that has a bearing on the reliability of the inversion for the moment tensor is the condition number of the generalized inverse of the sensitivity matrix. The inversion scheme is usually of the form

$$\mathbf{d} = \mathbf{GM} \dots (2.1)$$

The moment tensor elements are then obtained from

$$\mathbf{M} = (\mathbf{G}^T \mathbf{G})^{-1} \mathbf{G}^T \mathbf{d} \dots (2.2)$$

where \mathbf{d} is a matrix amplitudes of the direct arrivals (both P-and S-waves), \mathbf{G} is the impulse response of the medium as the wave field moves from the source to the receiver. The condition number of the generalized inverse of \mathbf{G} can affect the stability of the inversion for \mathbf{M} . If the condition number is large, it implies the inversion is unstable and that the moment tensor elements obtained might not reflect the true nature of the source mechanism. The condition number has been shown to have a connection with the solid angle subtended by the receiver array as viewed from the source. (Eaton, 2009)

The solid angle Ω is given by

$$\Omega = \int_S \frac{\mathbf{r} \cdot \hat{\mathbf{n}}}{r^3} dS \dots (2.3)$$

where $r = |\mathbf{r}|$ is the radial source to receiver distance, and $\hat{\mathbf{n}}$ is a vector normal to the receiver and directed at the source. (Eaton and Forouhideh, 2011) A plot of condition number against solid angle shows that the condition number has an inverse relationship with the solid angle subtended by the receiver array.

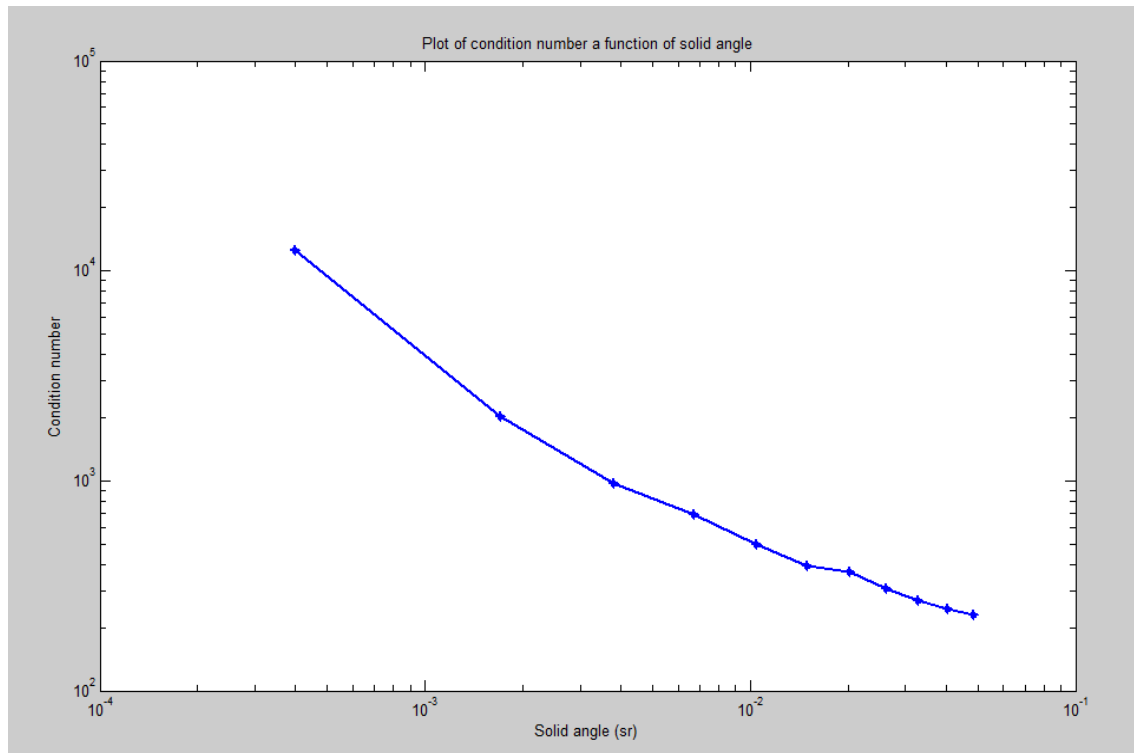


Figure 2.1: Condition number as a function of solid angle (Adapted from Eaton, 2009)

Even though the general consensus seems to be that it is not possible to reliably invert for the moment tensor elements from a single borehole, the paper by Song and Toksöz (2011) have a different opinion. They were able to show that, using full waveform information, the elements of the moment tensor can be retrieved from events

that are close to the monitoring well. Their study revealed that at near field range (i.e. a source – receiver distance that is less than five times the wavelength of the dominant S-wave) the condition number of the sensitivity matrix for a single borehole scenario is no different from that of a multiple borehole case.

2.5 GRAPHICAL REPRESENTATION OF SOURCE MECHANISM

There is an old saying that “a picture is worth a thousand words”, meaning that that the complexity of an idea can be drastically reduced if the idea can be portrayed pictorially. This is no different with the concept of source mechanism. A number of ingenious ways have been devised of portraying source mechanism, two of which are discussed below:

2.5.1 BEACH BALL DIAGRAMS:

Beach ball diagrams are lower hemisphere stereographic projections that are each divided up into four quadrants, two white and the other two black, separated by two great circles normal to each other. They are constructed by means of an equal area stereonet (figure 2.2) or a Schmidt projection. (Stein and Wysession, 2003)

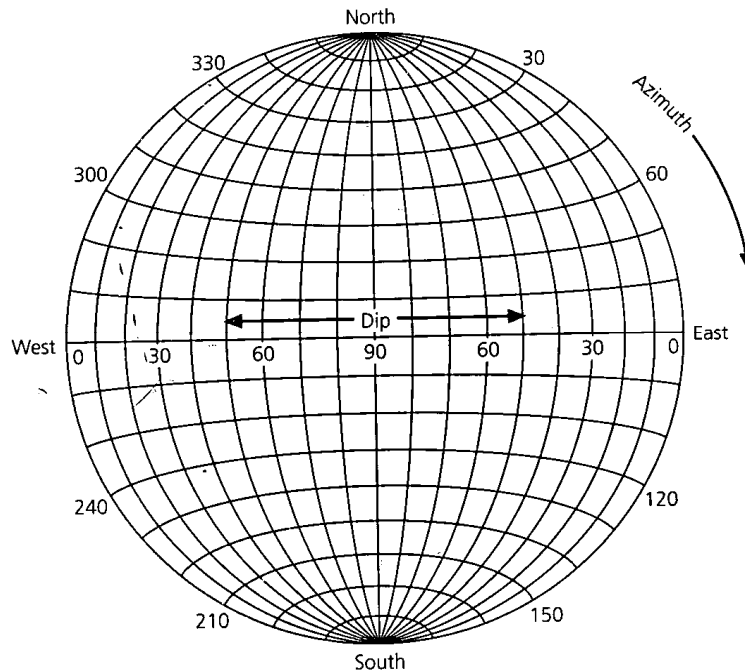


Figure 2.2: An equal area stereonet.

On the stereonet, the azimuth of the propagating wave is represented by the numbers 0° to 360° around the circumference, while the dip angle of the fault plane is represented by the numbers 0° to 90° on the net's equatorial axis. To plot the beach ball diagram of an event, we need the azimuth and the take-off angle of the seismic waves radiated from the source, as well as the polarity. A detailed description of how to plot beach ball diagrams is to be found in Stein and Wysession (2003). An example of beach ball representations of the three typical source mechanisms and their associated moment tensors are shown in figure 2.3.

Mechanism	Beach ball	Moment Tensor	Beach ball	Moment Tensor
Isotropic		$\frac{1}{\sqrt{3}} \begin{bmatrix} 1 & 0 & 0 \\ 0 & 1 & 0 \\ 0 & 0 & 1 \end{bmatrix}$		$-\frac{1}{\sqrt{3}} \begin{bmatrix} 1 & 0 & 0 \\ 0 & 1 & 0 \\ 0 & 0 & 1 \end{bmatrix}$
DC		$-\frac{1}{\sqrt{2}} \begin{bmatrix} 0 & 1 & 0 \\ 1 & 0 & 0 \\ 0 & 0 & 0 \end{bmatrix}$		$\frac{1}{\sqrt{2}} \begin{bmatrix} 1 & 0 & 0 \\ 0 & -1 & 0 \\ 0 & 0 & 0 \end{bmatrix}$
CLVD		$\frac{1}{\sqrt{6}} \begin{bmatrix} 1 & 0 & 0 \\ 0 & -2 & 0 \\ 0 & 0 & 1 \end{bmatrix}$		$\frac{1}{\sqrt{6}} \begin{bmatrix} -2 & 0 & 0 \\ 0 & 1 & 0 \\ 0 & 0 & 1 \end{bmatrix}$

Figure 2.3: Beach balls and their associated moment tensors (Adapted from Stein and Wyession, 2003)

2.5.2 SOURCE TYPE PLOT:

The source type plot is a two-dimensional graphical display of all the range of possible source mechanisms contained in a given data set. (Hudson *et al.*, 1989) The source type plot is obtained from the moment tensor by first performing a principle axes transformation of the moment tensor to obtain the isotropic part (this given by $3m = m_{11} + m_{22} + m_{33}$). (Baig and Urbancic, 2010) From this, we obtain the deviatoric moment tensor elements which are given by

$$m_1^* = m_{11} - m; m_2^* = m_{22} - m; m_3^* = m_{33} - m \dots (2.4)$$

The two parameters that are used for plotting the source type k and T are then obtained, where

$$k = \frac{m}{|m| + |m_3^*|} \dots (2.5a) \text{ and } T = \frac{2m_1^*}{|m_3^*|} \dots (2.5b)$$

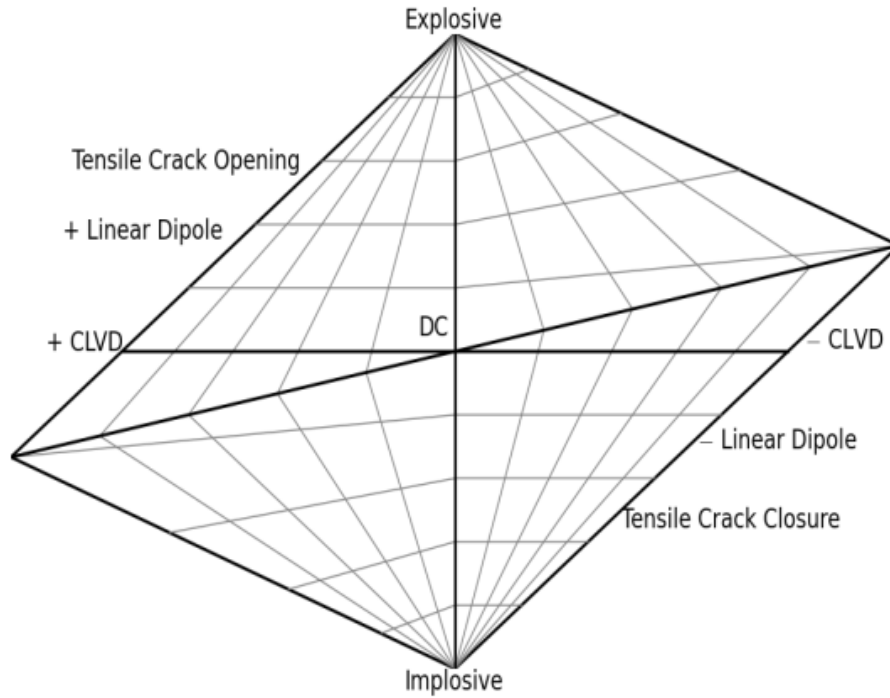


Figure 2.4: A source type plot (Courtesy Baig *et al.*, 2011)

k and T have values from -1 to 1 where $k = \pm 1$ (i.e., at the peak or base of the plot) correspond to purely explosive or implosive events respectively. (See figure 2.4)

$T = \pm 1$ correspond to positive or negative CLVD, while $k = T = 0$ correspond to pure double couple. Any values within the above mentioned range (i.e., that falls within the above figure) implies that the signal is a combination of two or more mechanisms.

Chapter Three

3.1 INTRODUCTION

The dataset used for this project was recorded during the hydraulic fracture treatment of a shale play in the Barnett, located at the north of Texas. A schematic diagram of the data acquisition geometry is shown in figure 3.1. The monitoring well is stationed 533 m from the treatment well. Contained in the monitoring well are a receiver string of twelve 3-component geophones located at a depth from 2100 m – 2270 m, with each geophones separated by about 12 m. There are two injection points in the treatment well located at depth about 2,149 m and 2,195 m.

○ Frac well(F) and Monitoring(M) well.

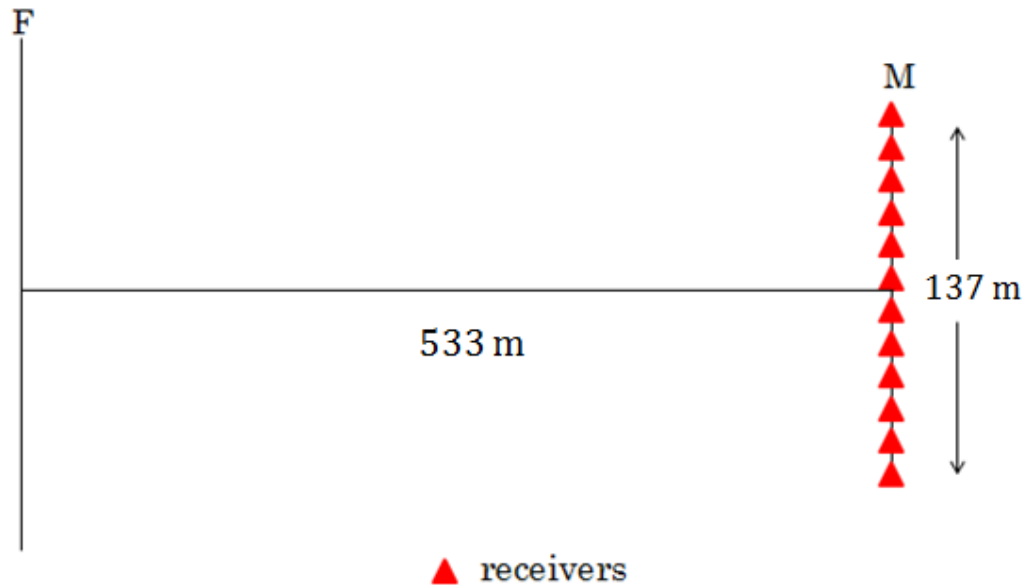


Figure 3.1: A schematic of the acquisition geometry of the microseismic events.

In the course of the hydraulic fracturing, over 10,000 microseismic events within the depth range 2,042 – 2,350 m were recorded. (Figure 3.2) The events, though, were predominantly within the depth range 2,195 – 2,286 m. As with most microseismic recordings, a large number of the signals were riddled with noise.

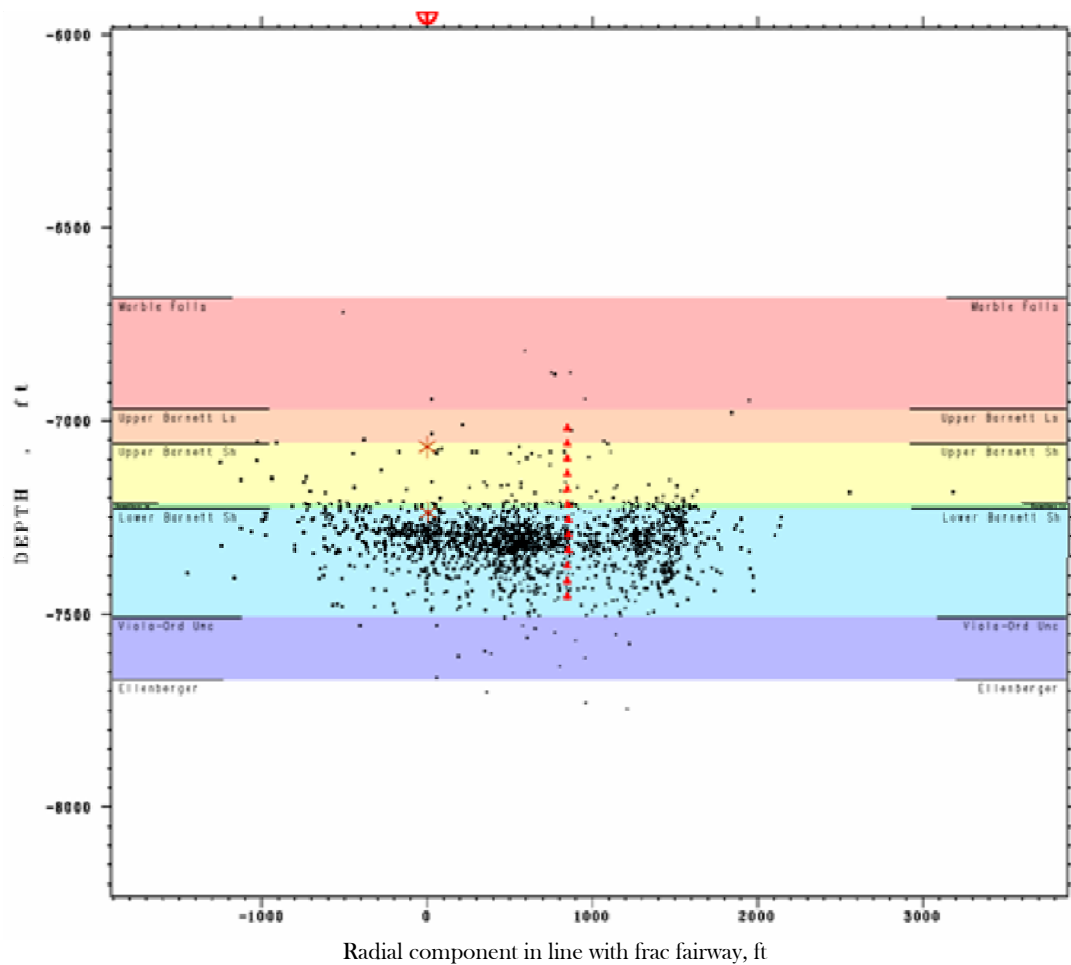


Figure 3.2: A cross section of the medium that was hydraulically fractured, and from which the microseismic events were recorded.

In some of the seismographs, the waveforms are so mumbled that it is difficult, if not impossible, to differentiate between the arrivals of the *P*-wave from that of the *S*-waveforms. (Figure 3.3a)

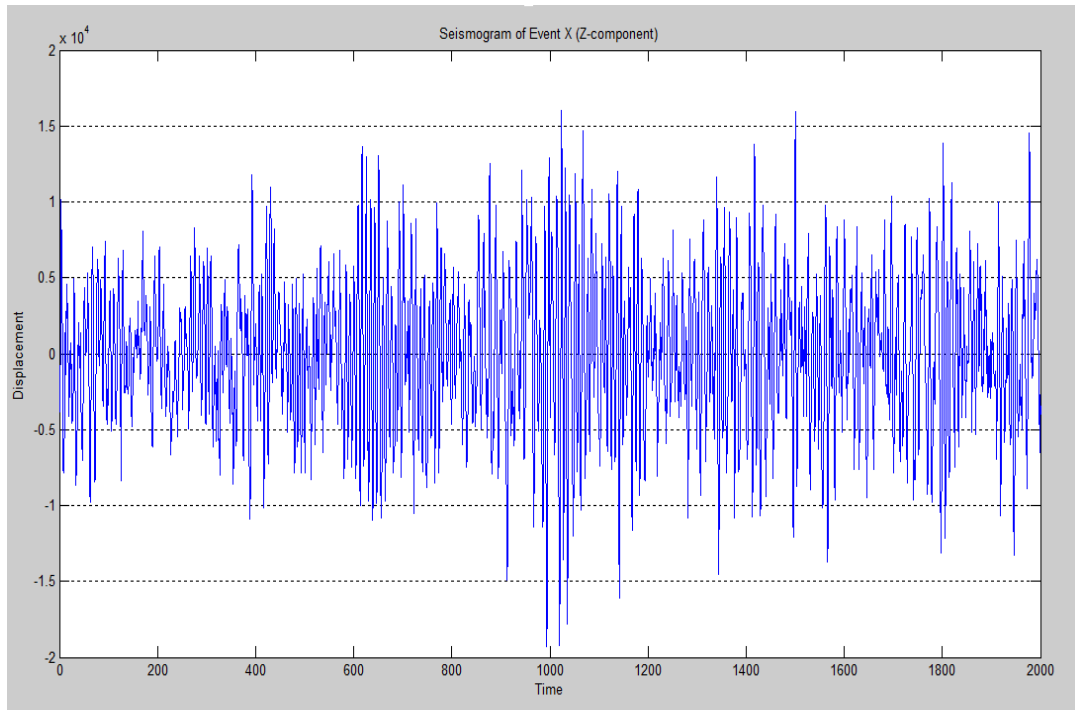


Figure 3.3a: Waveform of Event X (Very noisy)

There are also some of the signals that are quite neat such that, you could see the waveform of the different arrivals. (Figure 3.3b)

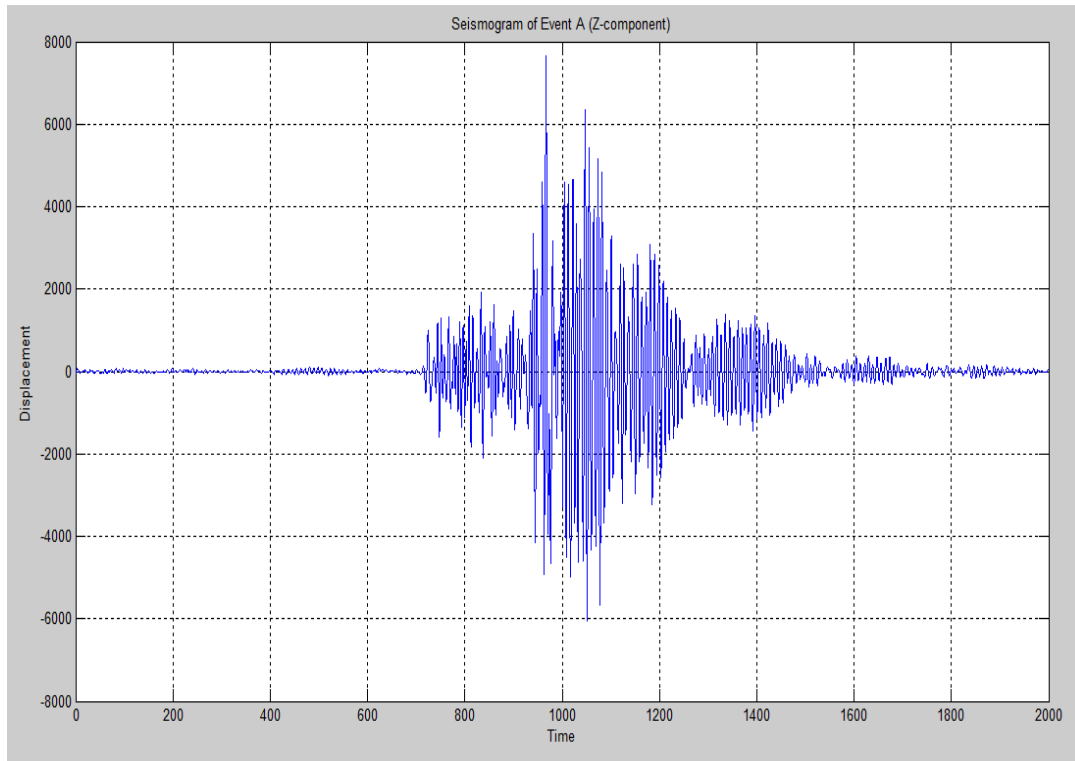


Figure 3.3b: Waveform of Event A

3.2 ANALYSIS OF THE DATA

Since the receivers are three component geophones, displacements are measured in three mutually perpendicular direction, namely, N – S, E – W and Z (i.e. vertical) component. Recall that the expression for the displacement field due to a moment tensor source is given by (Aki and Richards, 2002)

$$u_n(\mathbf{x}, t) = M_{ij} * G_{ni,j} \dots (3.1)$$

We note that the displacement is a three component vector, with a time component. Hence, for an elapsed time, t , there will be an array of three column vectors representing the displacement field at different points in time. For the dataset used in this study, there were two thousand time – sampled points.

The first task embarked upon was to look through the various events and see which of them lend itself to further analysis, or from which we can extract the source mechanism. Of the over ten thousand events recorded, only about two hundred and fifty to three hundred events were of good enough quality.

3.3 POWER SPECTRAL DENSITY ANALYSIS

The power [or energy (the terms are interchangeable)] spectrum of a signal is a way of showing the distribution of the power of the signal among various frequencies. In it, we see the existence and relative power of repetitive patterns and/or random structures of a signal in the frequency domain. The most common method used in spectral energy estimation is based on fast Fourier Transform (FFT) algorithm. The FFT algorithm is mostly preferred because of its ability to reveal spectral structures that can be used to identify the features of a signal. (Vaseghi, 2008) A traditional method used in the estimation of the power spectral density of an N -sampled signal is that established by Sir Arthur Schuster, which is known as the periodogram. The periodogram of a signal $r(t)$ is defined as:

$$\hat{P}_{rr}(f) = \frac{1}{N} \left| \sum_{t=0}^{N-1} r(t) e^{-2\pi i f t} \right|^2 \dots (3.2)$$

$$= \frac{1}{N} |R(f)|^2 \dots (3.3)$$

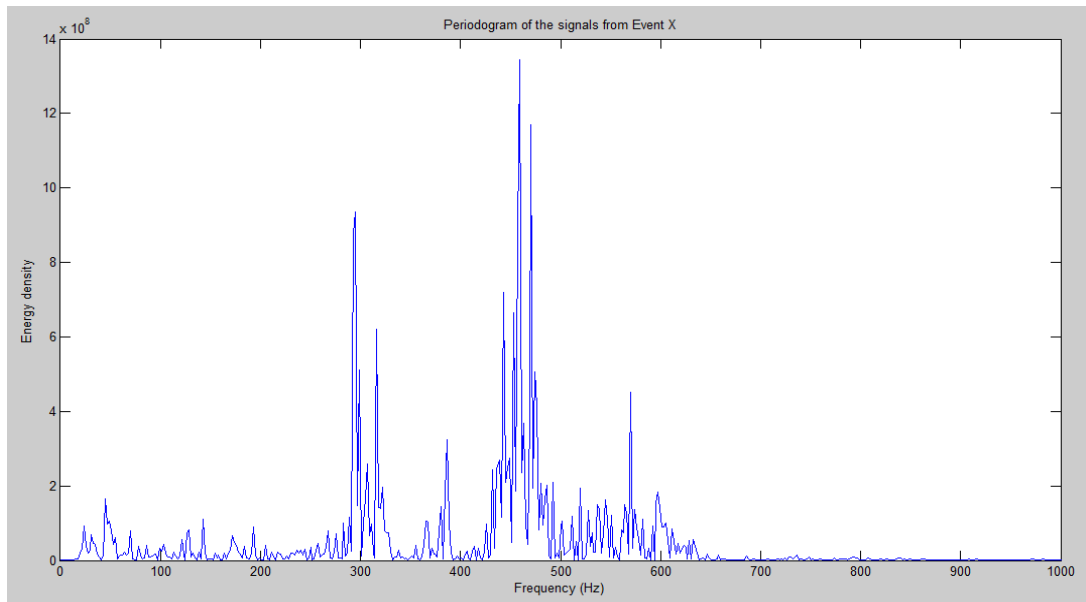


Figure 3.4a: Periodogram of event X for frequencies 0 - 1,000 Hz.

In order to gain insight into the nature of the signals present in the available dataset, a power spectral analysis was done on a number of the microseismic events. For this write up, the energy spectra of two events, one of very bad signal quality (Figure 3.3a), and the other with very good signal quality (Figure 3.3b), are presented here. At a glance, we see a marked difference between the spectra of event ‘A’ (clean signal) and event ‘X’ (noisy signal). To start with, the energy of the noisy signal is spread across a very broad range of frequencies compared to

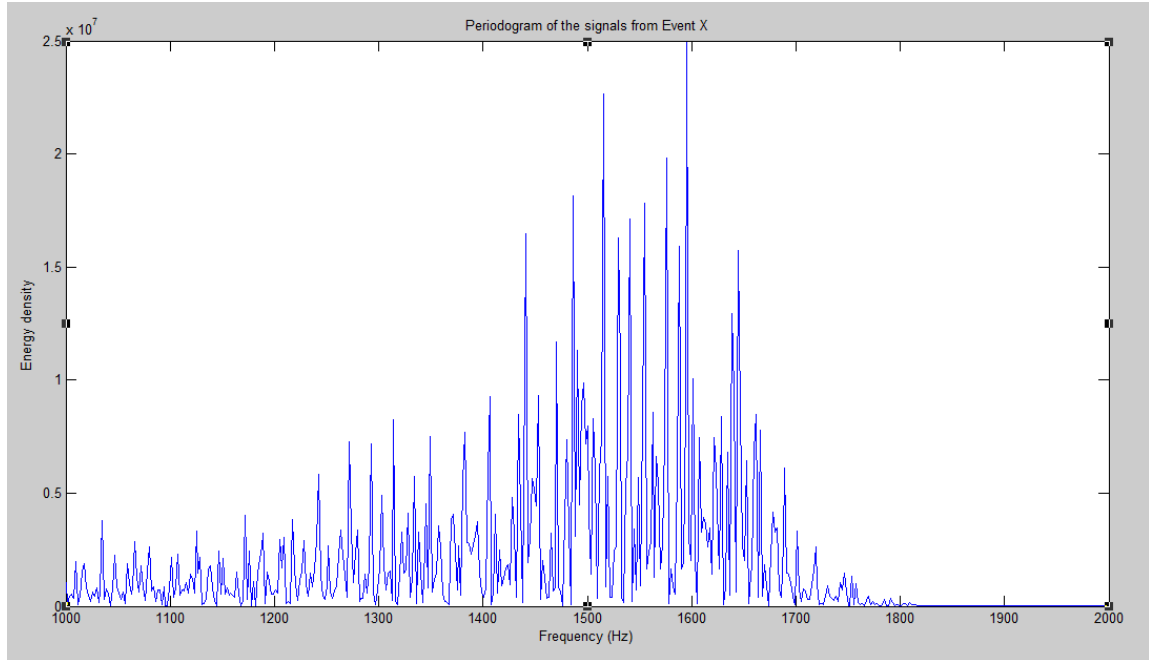


Figure 3.4b: Periodogram of event X for frequencies 1,000 - 2,000 Hz.

that of the clean signal, in which a significant part of the energy density lies between the frequency range 200 and 700 Hz (figures 3.4 and 3.5). One can therefore assume that the actual event lie somewhere in this frequency range. This makes events such as event A lend themselves to band pass filtering. The same cannot be said of events such as event X where the noise seems to spread over every frequency range. It might not be possible to filter such events without removing a significant part of the signals.

If we now take a close examination of the periodograms, we will also observe that the energy density of the noisy signal is higher than the energy spectra of the clean signal by an order of magnitude 10^2 .

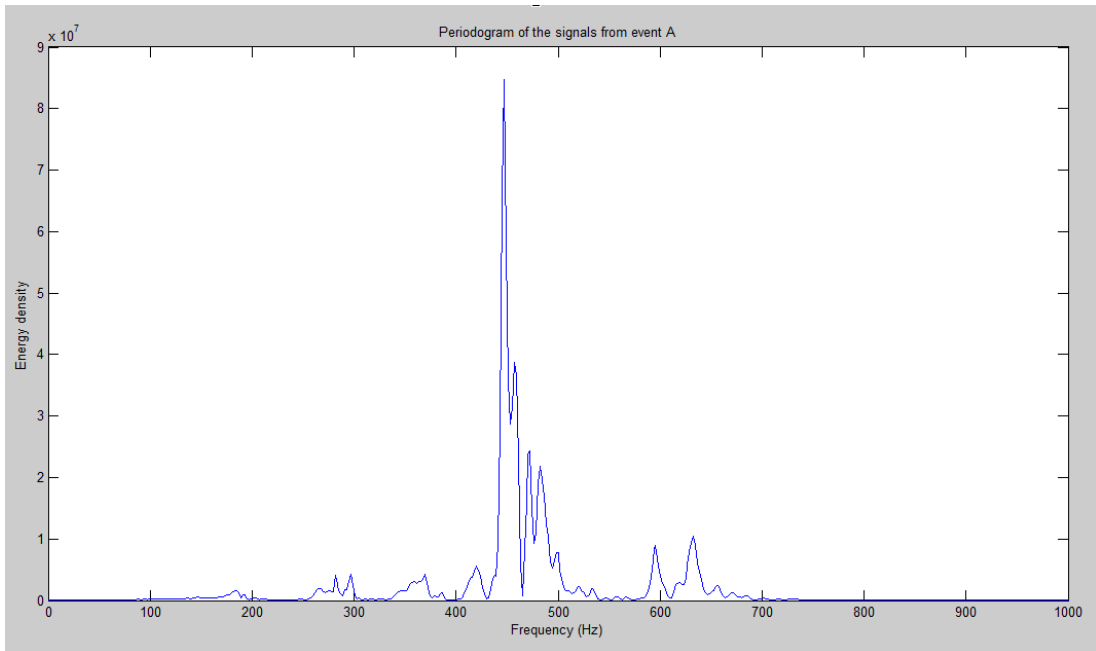


Figure 3.5a: Periodogram of event A for frequencies 0 - 1,000 Hz.

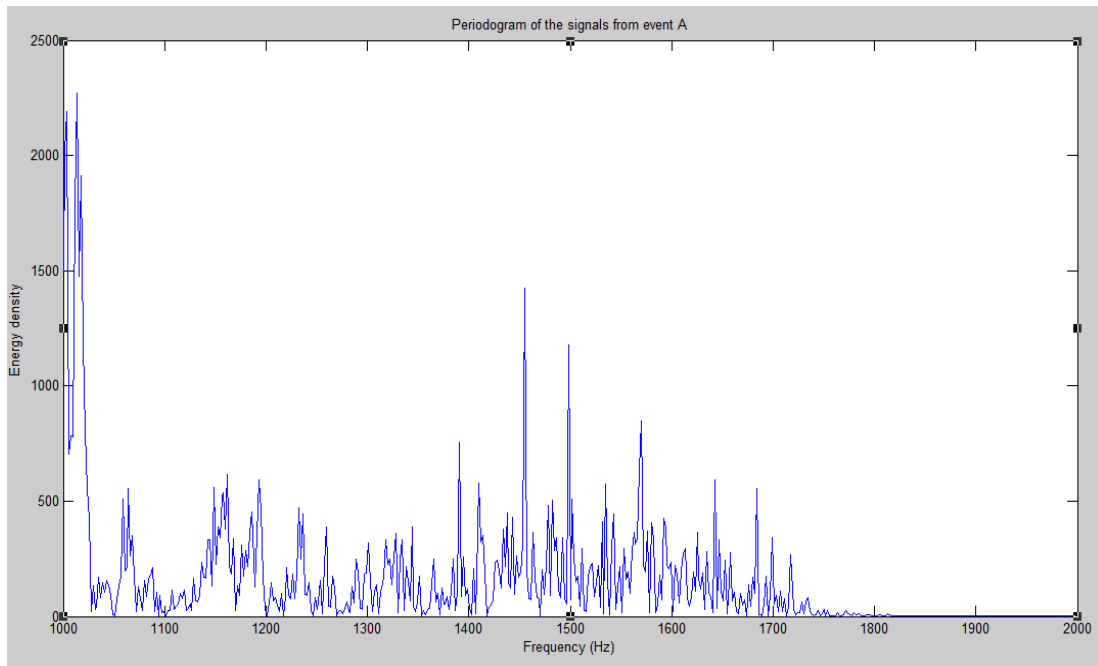


Figure 3.5b: Periodogram of event A for frequencies 1,000 - 2,000 Hz.

Bearing in mind that from the expression for the displacement field due to a moment tensor source, that the displacement $U_n(\mathbf{x},t)$ is a time varying function, if we subdivide the signals into different time segments, and perform the power spectral density of each segment, we see further difference between the signals of event A and X. (figures 3.6 and 3.7) From the periodogram, it appears there is no signal of significant energy density in the first quarter of recording for event A; the significantly energetic signals seems to reside in the second and third quarter of recording. In the case of event X, the signals seem to hit peak energy right from the onset; there is no point in time when the energy density is of an order less than 10^8 .

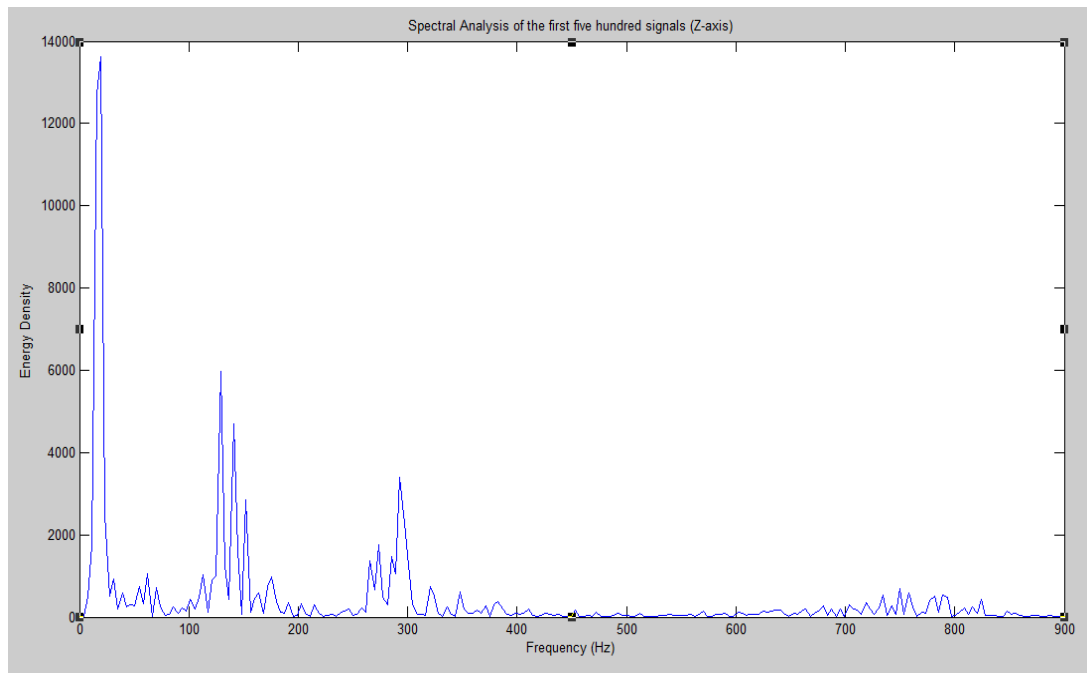


Figure 3.6a: Periodogram of first quarter time recording of event A.

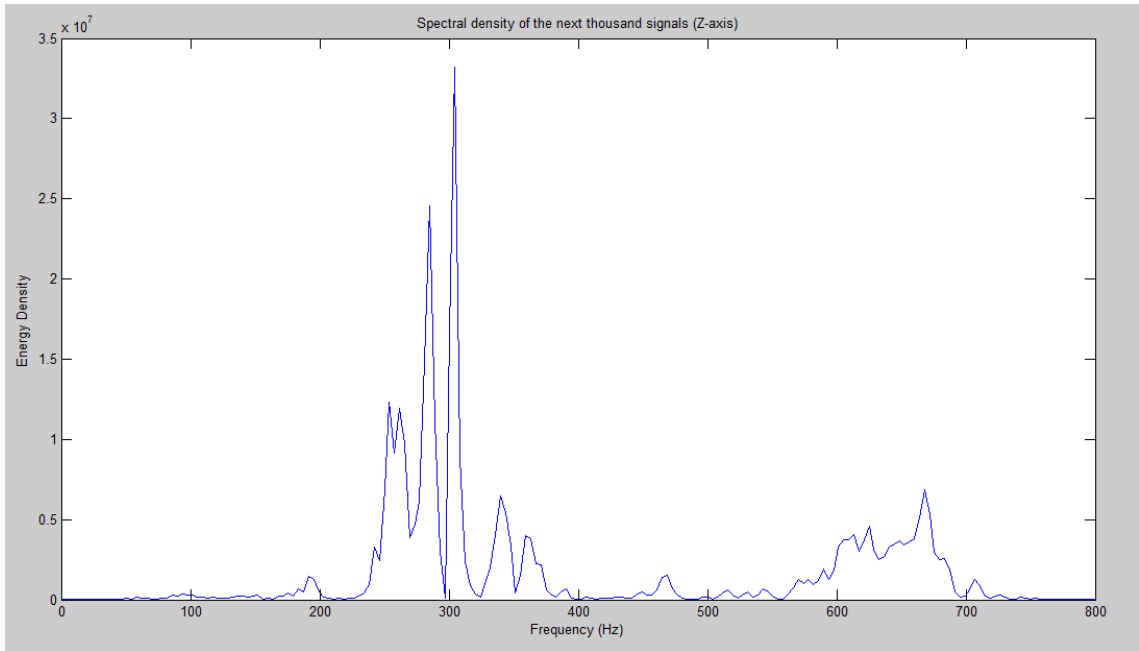


Figure 3.6b: Periodogram of second and third quarter time recording of event A.

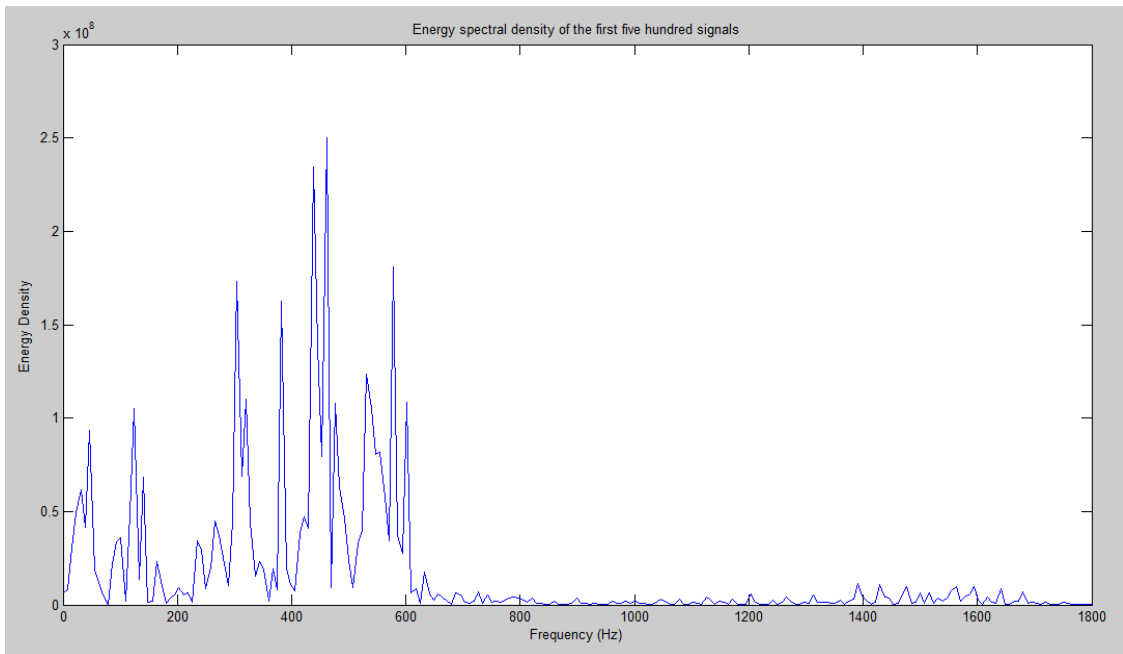


Figure 3.7a: Periodogram of first quarter time recording of event X.

The essence of these analyses is to determine from which of the over 10,000 events recorded we can perform an inversion to obtain the source mechanism. On analyzing the events, only a few were of good enough quality for inversion for the source mechanism.

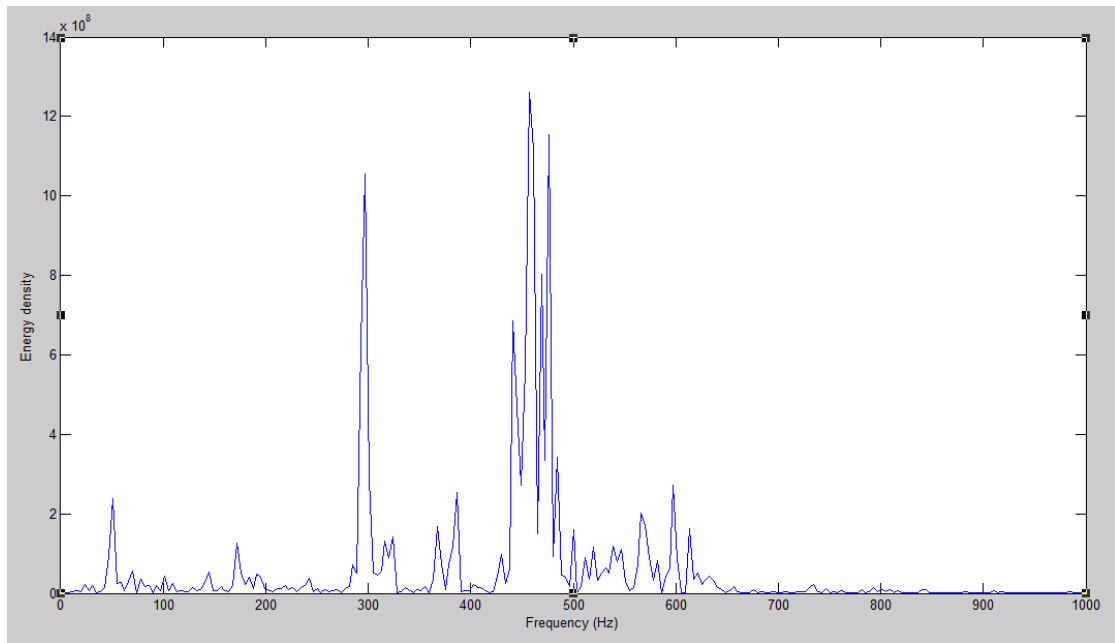


Figure 3.7b: Periodogram of second and third quarter time recording of event X.

However, there were some of the events whose quality could be enhanced by filtering. As an example, consider an event tagged “047”. A plot of this event before and after applying a band-pass filter to it is shown in figure 3.8. Figure 3.8a shows the vertical component, while fig. 3.8b shows the horizontal component.

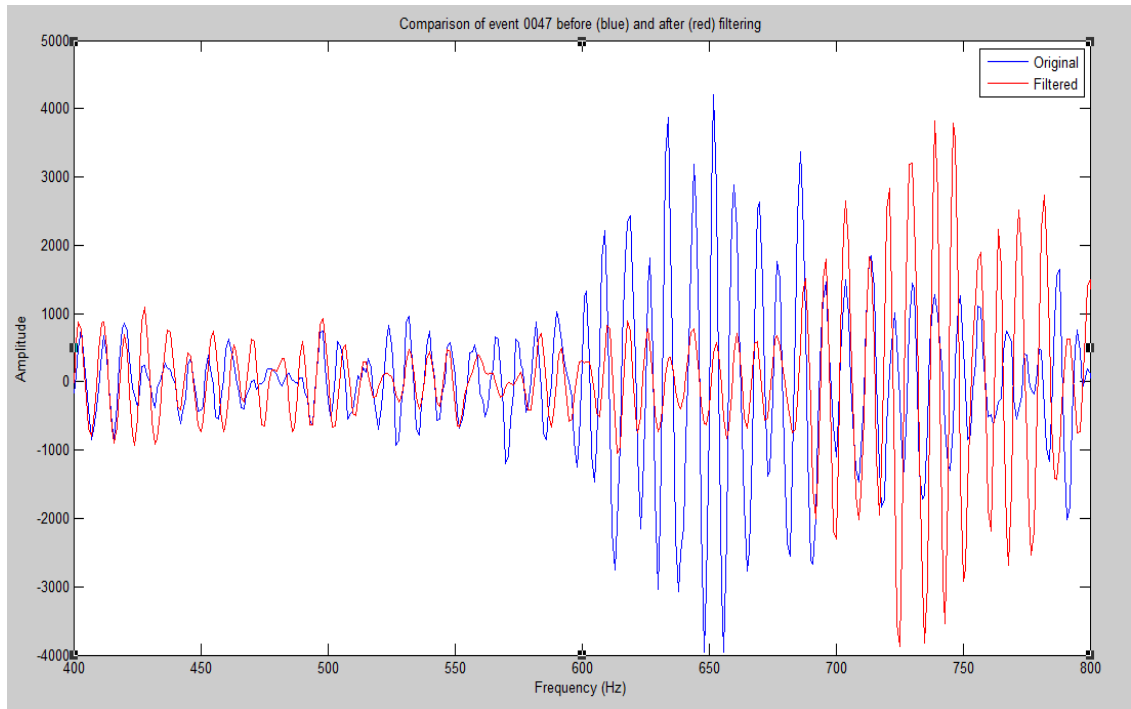


Figure 3.8a: Comparison of event 047 (Vertical component)

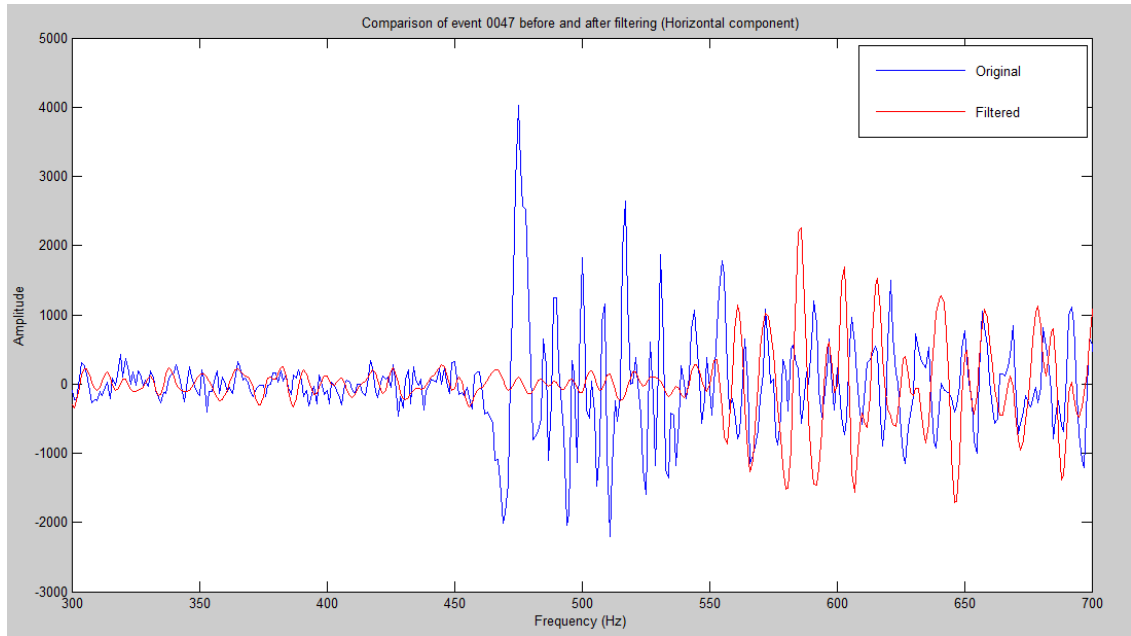


Figure 3.8b: Comparison of event 047 (Horizontal component)

3.4 THE ELASTODYNAMIC GREEN'S FUNCTION

It has been said that seismology is a “simple” science; there is the source, the medium and the receiver. (Chesnokov, personal interaction) In principle, the concept is that “simple”. In practice, however, there are a number of challenges, among which is how to determine the nature of the source, and the medium through which the wave field propagates from the source to the receivers. Most often, a pre-computed library of Green’s function (Rodriguez *et al.*, 2012; Li *et al.*, 2011, 2009), which is a description of the property of the medium, is used to invert for the moment tensor – a description of the source mechanism. The reliability of the moment tensor obtained depends, among other things, on how well the pre-computed Green’s function reflects the property of the medium where the wave field propagates. Consideration would have to be given as to whether the medium is homogenous or inhomogeneous, whether it is isotropic or anisotropic, and if anisotropic, the nature of the anisotropy. In this study, the Green’s function used is obtained from the solution of the elastic wave equation in isotropic and vertically transverse isotropic (VTI) medium.

3.4.1 THE EQUATION OF MOTION:

We start off with Newton’s second law of motion (1), and Hooke’s law (2)

$$ma_i = f_i \dots (3.4)$$

$$\sigma_{ij} = C_{ijkl}\varepsilon_{kl} = C_{ijkl} \frac{\partial u_k}{\partial x_l} \dots (3.5)$$

Noting that

$$a_i = \frac{\partial^2 u_i}{\partial t^2} \dots (3.6)$$

and that

$$f_i = \frac{\partial \sigma_{ij}}{\partial x_j} \dots (3.7)$$

If we put (2) in (4), and substitute the result and (3) in (1), we obtain, after some rearrangement

$$\rho \frac{\partial^2 u_i}{\partial t^2} = C_{ijkl} \frac{\partial^2 u_k}{\partial x_j \partial x_l} \dots (3.8)$$

Equation (5) is the elastic wave equation for a homogenous continuum. It is from the solution of this equation that we obtain the elastodynamic Green's function. For the isotropic case, we introduce the isotropic stiffness tensor

$$C_{ijkl} = \lambda \delta_{ij} \delta_{kl} + \mu (\delta_{ik} \delta_{jl} + \delta_{il} \delta_{jk}) \dots (3.9)$$

If we put this in (5), and after some algebraic steps, we obtain

$$\rho \frac{\partial^2 u_i}{\partial t^2} = (\lambda + \mu) \frac{\partial^2 u_j}{\partial x_i \partial x_j} + \mu \frac{\partial^2 u_i}{\partial x_j^2} \dots (3.10)$$

Equation (7) is the elastic wave equation for a homogenous and isotropic medium. This equation has been solved analytically, and the Green's function obtained in the space – frequency domain is given by

$$G_{ij}(r, \omega) = \frac{1}{r} [h(\omega r)\delta_{ij} + g(\omega r)n_i n_j] \dots (3.11)$$

where

$$h(\omega r) \equiv \frac{1}{4\pi\rho\omega^2 r^2} \left\{ \left[\left(1 + \frac{i\omega r}{V} \right) e^{i\omega r/V} \right]_{V_s}^{V_p} + \frac{r^2 \omega^2}{V_s^2} e^{-i\omega r/V_s} \right\} \dots (3.12)$$

$$g(\omega r) \equiv \frac{-1}{4\pi\rho\omega^2 r^2} \left\{ \left[3 \left(1 + \frac{i\omega r}{V} \right) - \frac{r^2 \omega^2}{V^2} \right] e^{-i\omega r/V} \right\}_{V_s}^{V_p} \dots (3.13)$$

and $n_i \equiv r_i/r$ where r_i is the i th component of the vector r .

Equation 8 – 10 is the dynamic Green's function for a homogenous and isotropic medium. [The reader who is interested in the complete steps leading up to the above Green's function can see appendix A of Tiwary *et al.*, (2009)].

While it is easier to think of an isotropic earth, it is not realistic to do so, especially when the medium to be modeled is a shale formation. Hence, the Green's function for anisotropic medium will also be considered. Anisotropy can be very difficult to deal with because the elastic parameters required to define it can be as many as eighty-one (81), but exploring the symmetry of stresses and strains, as well as the existence of a unique strain energy potential, brings the required elastic parameters

down to, at most, twenty-one (Mavko *et al.*, 2003). Depending on the kind of symmetry in question, we can require as little as three independent parameters to characterize an anisotropic medium. In this study, the symmetry of choice is the hexagonal (or transversely isotropic) symmetry. There are two reasons for choosing this symmetry. For one, this is the kind of anisotropy that is very common in sedimentary rocks at long wavelengths. The other reason is that the analytic solution of the dynamic Green's function for the transversely isotropic symmetry has been solved. The Green's function, being a symmetric tensor, has six independent elements, which are given in the $k - \omega$ (Zhao Li, Personal interaction) as

$$G_{11} = \frac{-(\rho\omega^2 - C_{44}k_r^2 - C_{33}k_3^2)}{(\rho\omega^2 - \rho k^2 V_p^2)(\rho\omega^2 - \rho k^2 V_{s1}^2)} \cos^2 \varphi - \frac{1}{\rho\omega^2 - \rho k^2 V_{s2}^2} \sin^2 \varphi \dots (3.14a)$$

$$G_{22} = \frac{-(\rho\omega^2 - C_{44}k_r^2 - C_{33}k_3^2)}{(\rho\omega^2 - \rho k^2 V_p^2)(\rho\omega^2 - \rho k^2 V_{s1}^2)} \sin^2 \varphi - \frac{1}{\rho\omega^2 - \rho k^2 V_{s2}^2} \cos^2 \varphi \dots (3.14b)$$

$$G_{33} = -\frac{1}{\det(A_{ij})} \rho(\rho\omega^2 - k^2 \Gamma_{11})(\omega^2 - k^2 V_{s2}^2) \dots (3.14c)$$

$$G_{12} = \left[\frac{-(\rho\omega^2 - C_{44}k_r^2 - C_{33}k_3^2)}{(\rho\omega^2 - \rho k^2 V_p^2)(\rho\omega^2 - \rho k^2 V_{s2}^2)} \right] \sin \varphi \cos \varphi \dots (3.14d)$$

$$G_{13} = -\frac{1}{\det(A_{ij})} k_1 k_3 (C_{13} + C_{44}) (\rho \omega^2 - \rho k^2 V_{s2}^2) \dots (3.14e)$$

$$G_{23} = -\frac{1}{\det(A_{ij})} k_2 k_3 (C_{13} + C_{44}) (\rho \omega^2 - \rho k^2 V_{s2}^2) \dots (3.14f)$$

where

$$A_{ij} = \rho \delta_{ij} \omega^2 - C_{ijkl} k_k k_l \dots (3.15)$$

$$\Gamma_{ij} = C_{ijkl} n_k n_l \dots (3.16)$$

The expression for the dynamic Green's function shows that an important aspect of source parameter estimation is the velocity model used for the inversion. Some studies have shown that an error in the velocity model used also translates to an error in the Green's function, which in turn results in errors in the estimated source parameters. (Rodriguez *et al.*, 2012)

3.5 FOCAL MECHANISM DETERMINATION OF THE EVENTS

3.5.1 ISOTROPIC CASE:

The determination of the focal mechanism of the recorded microseismic events, represented by the second rank symmetric tensor will proceed in two path way. There will be an inversion that will be constrained to zero trace, and the other will be unconstrained. The velocity model for the isotropic case is shown in figure 9. Events A and 047 will be used as sample of how the inversion was carried out in the other events.

The Green's function was calculated for an isotropic medium using equation 8 – 10.

The source time function used was a smooth ramp with a centre frequency of 500 Hz.

(Song and Toksöz, 2011) The Green's function was then inverse Fourier transformed so as to perform a linear time domain moment tensor inversion. (Pasyanos *et al.*, 1996)

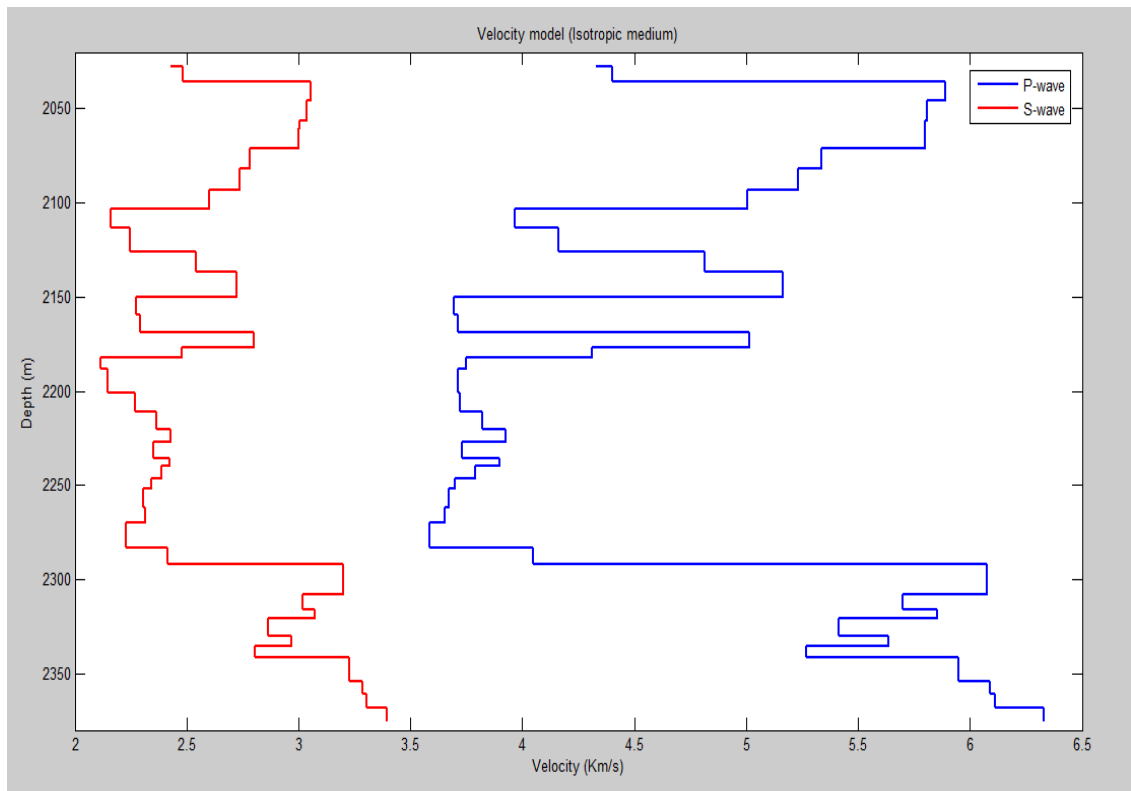


Figure 3.9: Velocity model for the Isotropic case

For event 'A', the moment tensor obtained from the inversion was

$$\mathbf{M}(A) = \begin{bmatrix} 0.0224 & 0.0013 & 0.0172 \\ 0.0013 & 0.5574 & -0.1599 \\ 0.0172 & -0.1599 & 0.8230 \end{bmatrix}$$

But unfortunately, the condition number was way too high (about 3868) to inspire any confidence in the result. However, on constraining the inversion to a deviatoric (i.e. imposing a zero trace) moment tensor such that elements of the moment tensor would be of the form (Nolen-Hoeksema and Ruff, 1999)

$$\mathbf{M}(A) = \begin{bmatrix} M_{11} & M_{12} & M_{13} \\ M_{12} & M_{22} & M_{23} \\ M_{13} & M_{23} & -(M_{11} + M_{22}) \end{bmatrix}$$

The moment tensor obtained in this instance was

$$\mathbf{M}(A) = \begin{bmatrix} 0.3554 & 0.0013 & 0.0172 \\ 0.0013 & 0.0898 & -0.1599 \\ 0.0172 & -0.1599 & -0.4452 \end{bmatrix}$$

The condition number for the constrained inversion was 468. This is way better than that obtained for the unconstrained inversion, and does inspire a measure of confidence in the result obtained.

3.5.2 VERTICAL TRANSVERSE ISOTROPIC (VTI) CASE:

As mentioned earlier, isotropy does not reflect the true nature of the earth's subsurface; it certainly is not a true reflection of a shale formation where anisotropic has been shown to be very pronounced (Khan *et al.*, 2011, Lonardelli *et al.*, 2007) The type of anisotropic used for building the model is the VTI model, in which case there are three modes of propagation which are mutually orthogonal in their polarization. The velocities of the three modes of propagation are given by

$$V_p^2 = V_{po}^2 [1 + 2\delta \sin^2\theta + 2(\varepsilon - \delta) \sin^4\theta] \dots (3.17)$$

$$V_{s1}^2 = V_{s0}^2[1 + 2\delta \sin^2\theta \cos^2\theta + 2\varepsilon \sin^4\theta] \dots (3.18)$$

$$\rho V_{s2}^2 = C_{66} \sin^2\theta + C_{44} \cos^2\theta \dots (3.19)$$

where V_{p0}^2 and V_{s0}^2 are the isotropic velocities given by

$$V_{p0}^2 = \sqrt{\frac{C_{33}}{\rho}} \dots (3.20a) \text{ and; } V_{s0}^2 = \sqrt{\frac{C_{44}}{\rho}} \dots (3.20b)$$

and ε & δ are the Thompson's parameter which are given by

$$\varepsilon = \frac{C_{11} - C_{33}}{2C_{33}} \dots (3.21)$$

$$\delta = \frac{(C_{13} + C_{44})^2 - (C_{33} - C_{44})^2}{2C_{33}(C_{33} - C_{44})} \dots (3.22)$$

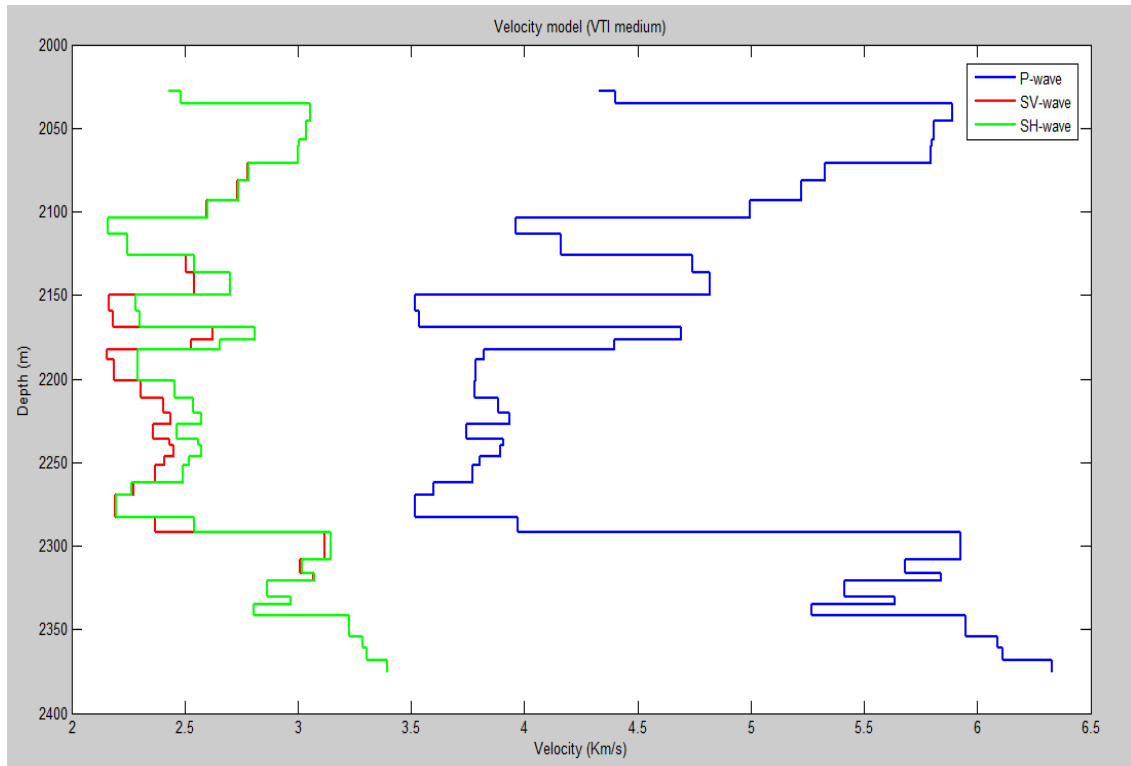


Figure 3.10: Velocity Model for the VTI Case

With these parameters, a velocity model for the VTI case was built, (Fig. 3.10) from which the Green's function is computed. As in the isotropic case, the Green's function was then inverse Fourier transformed so as to perform a linear time domain moment tensor inversion. The inversion for the source mechanism of event '047' was done for the VTI case and the moment tensor obtained was

$$\mathbf{M}(047) = \begin{bmatrix} 0.0030 & 0.0052 & -0.0147 \\ 0.0052 & 0.3373 & -0.2505 \\ -0.0147 & -0.2505 & 0.4590 \end{bmatrix}$$

With a condition of about 417, this inversion seem to more stable than when an isotropic medium is assumed. Moreover, when we now constrain out inversion to a deviatoric moment tensor, we obtain

$$\mathbf{M}^{\text{dev}}(047) = \begin{bmatrix} -0.2634 & 0.0052 & -0.0147 \\ 0.0052 & 0.0709 & -0.2505 \\ -0.0147 & -0.2505 & 0.1925 \end{bmatrix}$$

The condition number for this inversion was 168. This seems quite good in terms of reliability of the result. The eigenvalues for $\mathbf{M}^{\text{dev}}(047)$ are

$$\begin{bmatrix} -0.2639 \\ -0.1259 \\ 0.3898 \end{bmatrix}$$

From this, we compute the value of ε (see equation 1.9) as 0.32, from which we deduce that the percentage of CLVD in $\mathbf{M}^{\text{dev}}(047)$ is 64.6 % and that of DC is 35.4 %.

This inversion procedure was applied to about 100 other events, most of which had to be band pass filtered using the band 100 – 800 Hz. A majority of the event yielded a condition number that was below 1,000, while a few were had condition numbers that was way beyond 1,000.

Chapter Four

4.1 INTRODUCTION

The microseismic events recorded off a Barnett shale play was subjected to power spectral density analysis, as well as inversion for the source mechanism in order to determine the nature or mode of failure responsible for the observed wave field. The analysis of the spectra of one of the clean events (event A) clearly show that the peak energy of the wave field is to be found within the frequency range 400 – 500 Hz, and the next significant peak is in the range 600 – 700 Hz. While some of the other neat events follow the same feature as event ‘A’, some other neat events peak at the range 200 – 300 Hz. As an example, consider Event ‘B’ (Figure 4.1) which has a waveform that is as neat as the waveform of event A. (figure 3.3b) When we do a power spectral analysis of event B, we observe similar peaks as are seen in event ‘A’ (figure 4.2a), but unlike event A, they occur at the range 200 – 400 Hz. Also, like event ‘A’, event ‘B’ has no significantly large energy density observed beyond 1000 Hz. (Figure 4.2b)

These energy peaks seem to represent the energies of the P- and S-wave signals. No such distinct peaks are observed in the power spectral analysis of the signal of the noisy events.

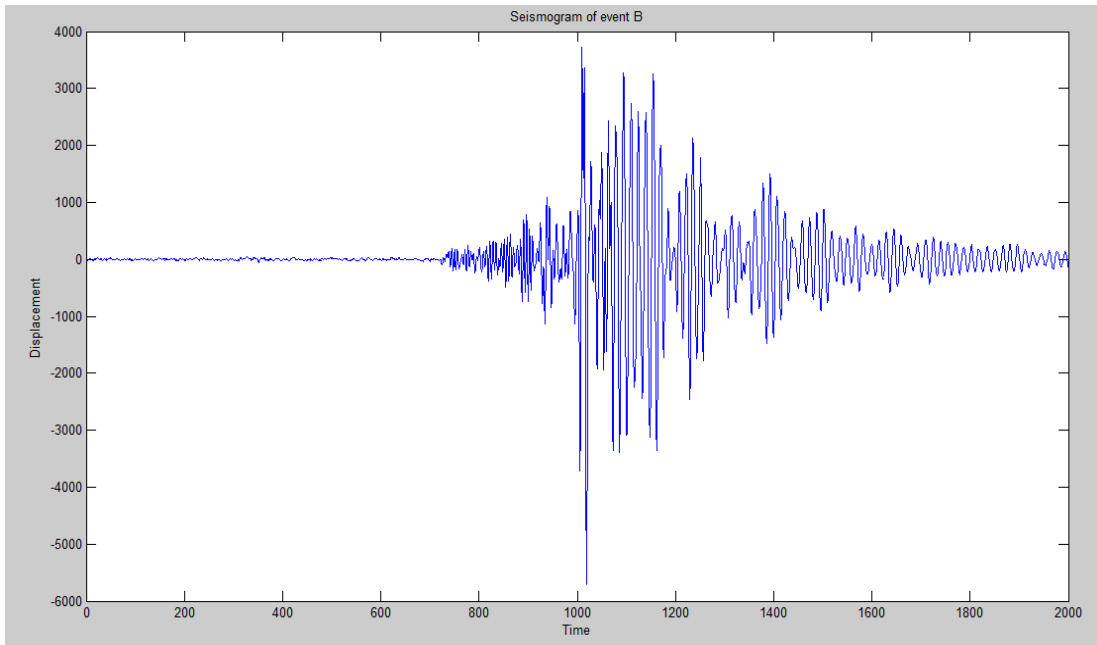


Figure 4.1: Waveform of Event B

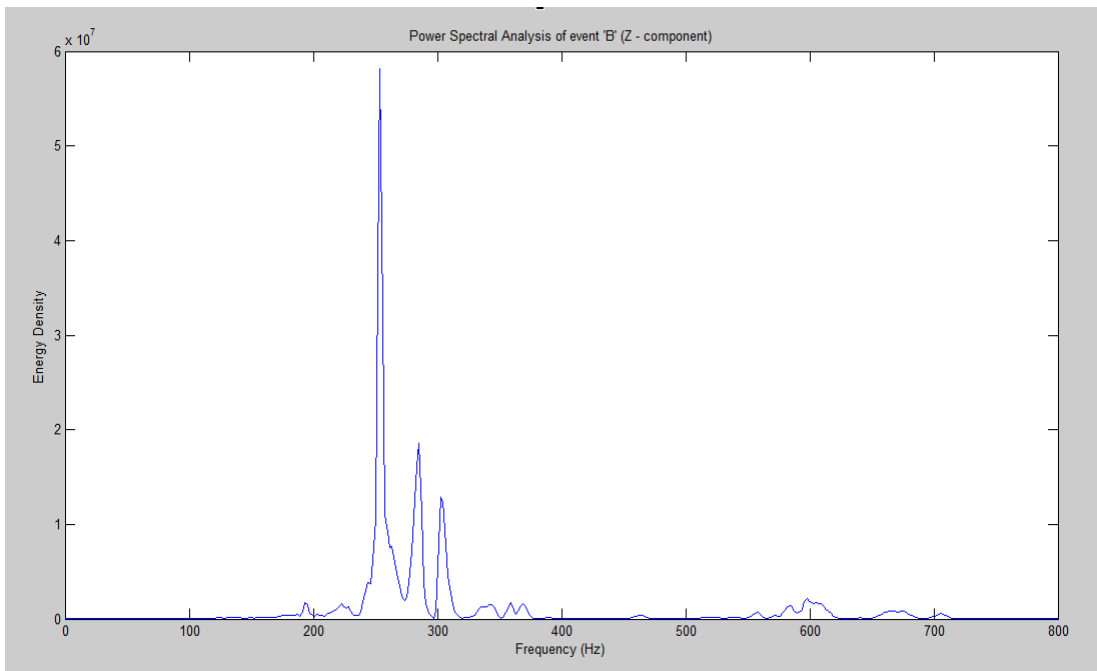


Figure 4.2a: Periodogram of event 'B' for frequencies 0 - 800 Hz.

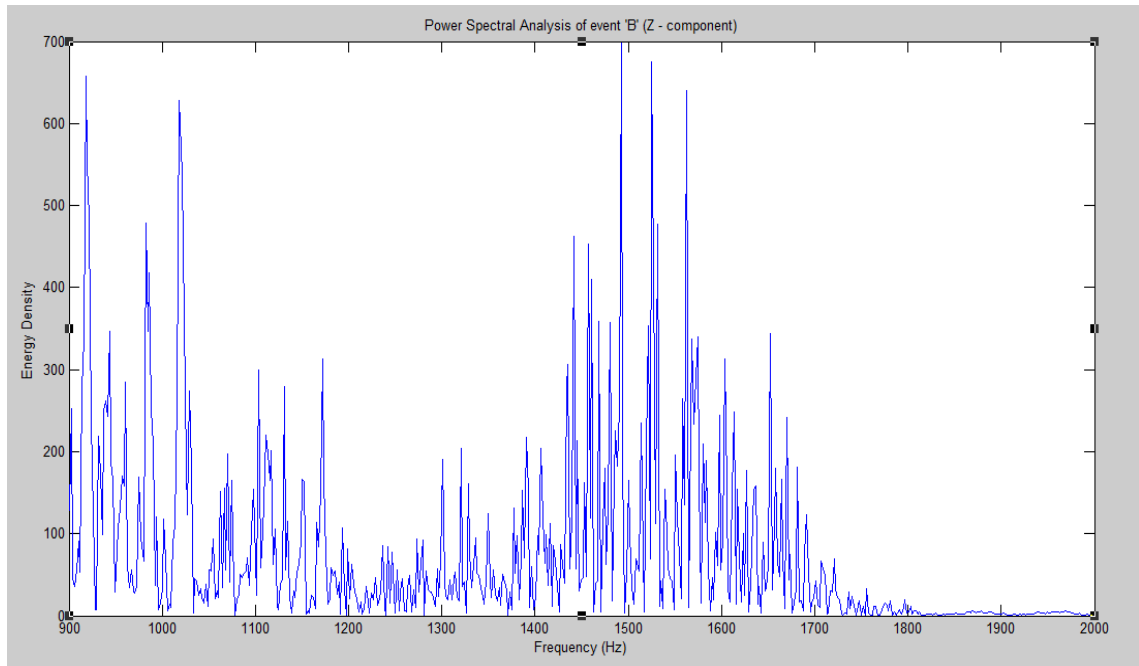


Figure 4.2b: Periodogram of event 'B' for frequencies 900 – 2,000 Hz.

4.2 ANALYSIS OF RESULTS

The power spectral density analysis of the signals from the microseismic events was meant to reveal the frequency content of the seismic signals. Armed with the information from the analysis, a band pass filter was designed so as to enhance those events whose signals were not of good quality. Only about 100 events were used to invert for the source mechanism, and the inversion was done for both isotropic and vertical transverse isotropic (VTI) medium. For instance, the inversion for event 'A' yielded the following moment tensors; for the inversion for the full moment tensor in VTI medium, the moment tensor obtained was

$$\mathbf{M}(A) = \begin{bmatrix} 0.0418 & -0.0017 & -0.0086 \\ -0.0017 & 0.5574 & -0.0585 \\ -0.0086 & -0.0585 & 0.1103 \end{bmatrix}$$

while the inversion for the deviatoric moment tensor yielded

$$\mathbf{M}^{dev}(A) = \begin{bmatrix} -0.1947 & -0.0017 & -0.0086 \\ -0.0017 & 0.3209 & -0.0585 \\ -0.0086 & -0.0585 & -0.1262 \end{bmatrix}$$

For this inversion, the condition number went from 356 to 92. For the moment tensor

$\mathbf{M}^{dev}(A)$, the eigenvalues are

$$\begin{bmatrix} -0.1959 \\ -0.1325 \\ 0.3284 \end{bmatrix}$$

From this, we compute ε to be 0.40, and from which it was determined that $\mathbf{M}^{dev}(A)$ has 20 % DC and 80 % CLVD. This deviatoric moment tensor was then decomposed into a compensated linear vector dipole given by

$$\mathbf{M}^{CLVD}(A) = \begin{bmatrix} -0.1262 & 0 & 0 \\ 0 & 0.2524 & 0 \\ 0 & 0 & -0.1262 \end{bmatrix}$$

and four double couple, namely

$$\mathbf{M}^{DC1}(A) = \begin{bmatrix} 0 & -0.0017 & 0 \\ -0.0017 & 0 & 0 \\ 0 & 0 & 0 \end{bmatrix}$$

$$\mathbf{M}^{DC2}(A) = \begin{bmatrix} 0 & 0 & -0.0086 \\ 0 & 0 & 0 \\ -0.0086 & 0 & 0 \end{bmatrix}$$

$$\mathbf{M}^{DC3}(A) = \begin{bmatrix} -0.0685 & 0 & 0 \\ 0 & 0.0685 & 0 \\ 0 & 0 & 0 \end{bmatrix}, \text{ and}$$

$$\mathbf{M}^{DC4}(A) = \begin{bmatrix} 0 & 0 & 0 \\ 0 & 0 & -0.0585 \\ 0 & -0.0585 & 0 \end{bmatrix}$$

While most of the events analyzed yielded similar mechanisms, some yielded slightly different mechanisms. In all, the result of the inversion for the source mechanisms reveal that the rock failures were predominantly due to shear failures (double couple) with a few non-shear failures such as vector dipoles and compensated linear vector dipoles (CLVD).

The inversion scheme that assumes a VTI medium yielded a result that is more stable than for an inversion scheme that assumes the medium is isotropic. Also, the inversion for the full moment tensor yielded a less reliable result in both media than the inversion for the deviatoric moment tensor. Studies involving the full moment tensor inversion and its deviatoric counterpart have been shown to yield larger values for the moment in the full moment tensor inversion than in the deviatoric case, and this was taken to indicate that the full moment tensor might be invalid! (Minson and Dreger, 2008)

Chapter Five

5.1 INTRODUCTION

The monitoring of micro-seismicity caused by hydraulic fracturing, and other man-made processes is important in understanding the propagation and network of fractures, which in turn helps enhance reservoir production. The inversion for the moment tensor plays a crucial role in identifying the differences in the stress field of the formation. To resolve the six independent constants of the moment tensor requires the total amplitudes of the P- SV-, and SH waves, (Baig and Urbancic, 2010) which are of good quality and that are noise-free. (Zimmer, 2011; Vavryčuk, 2007)

The high values of the condition number of the inversion matrix are attributable to the single azimuth data used for this study. Other studies done on the inversion for the moment tensor suggests that the inversion is more stable if the solid angle observed at the receivers when viewed from the source is greater than zero. (Eaton and Forouhideh, 2011)

5.2 CHALLENGES:

A vast majority of authors on the inversion of moment tensor agree that it is impossible to obtain the six independent components of the moment tensor from data acquired from an array of geophones in a single borehole. (Eaton and Forouhideh, 2011; Baig and Urbancic, 2010; Vavryčuk, 2007; Nolen-Hoeksema and Ruff, 2001; Nolen-Hoeksema and Ruff, 1999) The data used for this project were acquired from a string of

twelve 3-component geophones in a single borehole. This raises questions about the quality of the moment tensors obtained from inversion from such an array of geophones in a single borehole. The best quality of the moment tensor that can be achieved from inversion, barring the absence of accurate amplitude information depends, to a large extent, on how wide the ray paths travel from source to receiver. And of course, this requires information from receivers deployed in, at least two boreholes. (Zimmer, 2011; Vavryčuk, 2007)

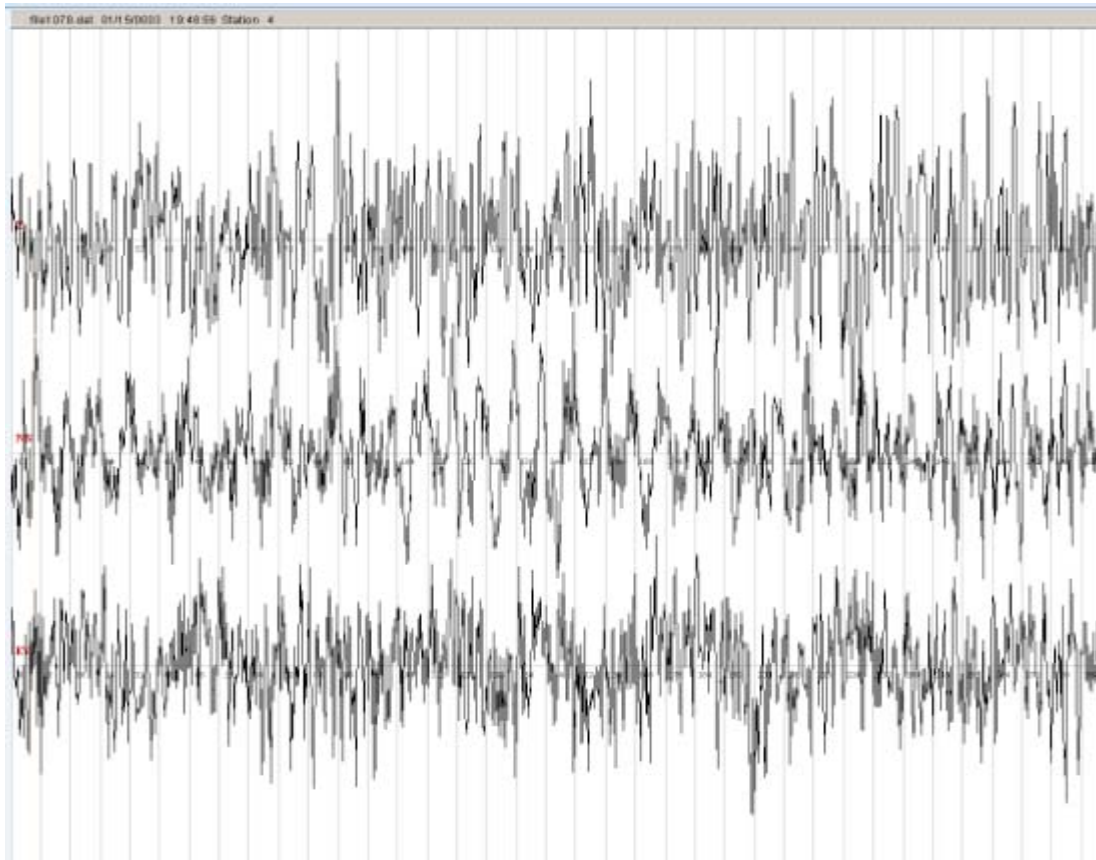


Figure 5.1: Typical nature of most of the data.

Another challenge in inverting for the moment tensor is the fact that a lot of the events were riddled with lots of noise. (See figure 5.1) This creates the problem, among others, of picking the time of arrivals of the different wave types (P-, SV and SH).

5.3 RECOMMENDATIONS:

It seems that most microseismic data acquired back then (the one used for this study was acquired in 2003) was lacking in proper acquisition design. Even those data acquired with proper design, might not have taken into consideration the needs of estimating the source mechanism from inversion for the moment tensor. While having wells at different azimuth would be very desirable, there is the cost implication to consider. But having such multiple monitoring arrays provides, not only a means of obtaining the complete moment tensor, but also, a way of explaining the azimuthal variations in the observed wave forms. (Baig *et al.*, 2011)

References

- Aki, K., and P. Richards, 2002. Quantitative Seismology, University Science Books, Sausalito, CA.
- Baig, A., and T. Urbancic, 2010, Microseismic moment tensors: A path to understanding frac growth: *The Leading Edge*, **29**, 320 – 324, doi: 0.1190/1.3353729.
- Baig, A., T. Urbancic, S. Bowman, K. Buckingham, V. Shumila, 2011. Reliability of non-double couple components in microseismic moment tensors, *SEG Expanded Abstract*, 1683 – 1687.
- Chapman, C. H. and W. S. Leaney, 2012. A new moment tensor decomposition for seismic events in anisotropic media, *Geophysical Journal International*, **188**, 343 – 370.
- Charlez, P.A., 1997, Rock Mechanics: Petroleum Applications, Vol. 2, Editions TECHNIP.
- Eaton, D. W., 2009. Resolution of microseismic moment tensors: A synthetic modeling study, *SEG Expanded Abstract*, 3569 – 3573.
- Eaton, D.W., and F. Forouhideh 2011. Solid angles and the impact of receiver-array geometry on microseismic moment tensor inversion, *Geophysics*, **76**, WC77 – WC85.
- Gharti, H. N., V. Oye, D. Kühn, and P. Zhao, 2011. Simultaneous micro earthquake location and moment tensor estimation using time reversal imaging. *SEG Expanded Abstract*, 1632 – 1637.
- Gilbert, F. 1970. Excitation of normal modes of the earth by earthquake sources, *Geophysical Journal of the Royal Astronomical Society*, **77**, 883 – 914.
- Herrmann, R. B., 1975, A student's guide to P and S wave data for focal mechanism determination, *Earthquake Notes*, **46**, 29 – 39.
- Hudson, J. A., R. G. Pearce, and R. M. Rogers, 1989. Source type plot for inversion of the moment tensor, *Journal of Geophysical Research*, **94**, B1, 765 – 774.
- Jost, M. L., and R. B. Herrmann, 1989, A student's guide to and review of moment tensors: *Seismological Research Letters*, **60**, 237 – 257.
- Khan, S., S. Ansari, H. Han, and N. Khosravi, 2011. Importance of Shale Anisotropy in estimating in-situ stresses and wellbore stability analysis in Horn River basin, *SPE – Canadian Unconventional Resource Conference* Digital object identifier #: 10.2118/149433-MS
- Lay, T., and T. C. Wallace, 1995. Modern Global Seismology: Academy Press.
- Leaney, W. S., 2008. Inversion of microseismic data by least squares time reversal and waveform fitting. *SEG Expanded Abstract*, 1347 – 1351.

- Li, J., H. Zhang, H. S. Kuleli, and M. N. Toksöz, 2009. Focal mechanism determination using high frequency, full waveform information, *SEG Expanded Abstracts*, **28**, 2312 – 2316.
- Li, J., H. Zhang, H. S. Kuleli, and M. N. Toksöz, 2011. Focal mechanism determination of induced micro-earthquakes in an oil field using full waveforms from shallow and deep seismic networks, *Geophysics*, **76**, 87 – 101.
- Lonardelli, I., H. R. Wenk, and Y. Ren, 2007. Preferred orientation and elastic anisotropy in shales, *Geophysics* **72** (2) D33 – D40.
- Madariaga, R., 2007. Seismic source theory, in *Treatise on Geophysics*, 59 – 82, ed. Schubert, G., Elsevier, Amsterdam.
- Mavko, G., T. Mukerji, J. Dvorkin, 2003. *The Rock Physics Handbook – Tools for Seismic Analysis in Porous Media*, Cambridge University Press, Cambridge, UK.
- Minson, S. E, and D. S. Dreger, 2008. Stable inversions for complete moment tensors, *Geophysical Journal International*, **174**, 585 – 592.
- Nolen-Hoeksema, R.C. and Ruff L.J. 1999. Moment tensor inversion of microseismic events from hydro-fractures, *SEG Expanded Abstract*.
- Nolen-Hoeksema, R.C. and Ruff L.J. 2001. Moment tensor inversion of microseisms from the B-sand propped hydrofracture, M-site, Colorado. *Tectonophysics* **336**, 163–181.
- Pasyanos, M.E., Dreger, D.S. and Romanowicz, B., 1996. Toward real-time estimation of regional moment tensors, *Bulletin of Seismological Society of America*, **86** (5), 1255–1269.
- Rodriguez, V. I., M. Sacchi and Y. J. Gu, 2012. Simultaneous recovery of origin time, hypocenter location and seismic moment tensor using sparse representation theory, *Geophysical Journal International*, **188**, 1188 – 1202.
- Šíleny, J., D. P. Hill, L. Eisner, and F. H. Cornet, 2009. Non – double couple mechanisms of microearthquakes induced by hydraulic fracturing, *Journal of Geophysical Research*, **114**, B08307.
- Sipkin, S. A., 1982. Estimation of earthquake source parameters by the inversion of waveform data: synthetic waveforms, *Physics of the Earth and Planetary Interior*, **30**, 242 – 259.
- Sipkin, S. A., 1994, Rapid determination of global moment-tensor solutions, *Geophysical Research Letters*, **21**, 16, 1667–1670
- Song, F. and N. Toksöz, 2011. Full-waveform based complete moment tensor inversion and source parameter estimation from downhole microseismic data for hydro fracture monitoring, *Geophysics*, **76**, 6, 101 – 114.
- Stein, S. and M. Wysession, 2003, *An Introduction to Seismology, Earthquakes, and Earth Structure*, Blackwell Publishing, Malden MA.

- Tiwary, D. K., I. O. Bayuk, A. A. Vikhorev, and E. M. Chesnokov, 2009. Comparison of seismic upscaling methods: From sonic to seismic, *Geophysics*, **74**, 2, WA3 – WA14.
- Vavryčuk, V., 2007, On the retrieval of moment tensors from borehole data: *Geophysical Prospecting*, **55**, 381 – 391, doi: 10.1111/gpr.2007.55.issue-3.
- Wéber, Z, 2009. Estimating source time function and moment tensor from moment tensor rate functions by constrained L_1 norm minimization, *Geophysical Journal International*, **178**, 889 – 900.
- Zimmer, U., 2011. Microseismic design studies, *Geophysics*, **76**, 6, WC17 – WC25.